Petroleum Science 20 (2023) 3311–3336

Contents lists available at ScienceDirect

Petroleum Science

journal homepage: www.keaipublishing.com/en/journals/petroleum-science

Original Paper

Origin of carbonate minerals and impacts on reservoir quality of the Wufeng and Longmaxi Shale, Sichuan Basin

Yang Chen [a, b], Jian-Hua Zhao [a, b, *], Qin-Hong Hu [a, b], Ke-Yu Liu [a, b], Wei Wu [c], Chao Luo [c], Sheng-Hui Zhao [a, b], Yu-Ying Zhang [d]

[a] National Key Laboratory of Deep Oil and Gas, China University of Petroleum (East China), Qingdao, Shandong, 266580, China
[b] School of Geosciences, China University of Petroleum (East China), Qingdao, Shandong, 266580, China
[c] Shale Gas Research Institute, PetroChina Southwest Oil and Gas Field Company, Chengdu, Sichuan, 610051, China
[d] Northeastern University, School of Resources and Civil Engineering, Shenyang, Liaoning, 110000, China

ARTICLE INFO

Article history:
Received 28 October 2022
Received in revised form
5 February 2023
Accepted 8 August 2023
Available online 10 August 2023

Edited by Jie Hao and Teng Zhu

Keywords:
Carbonate minerals genesis
Diagenetic evolution
Carbonate mineral types
Reservoir quality
Wufeng and Longmaxi Shale

ABSTRACT

The Ordovician-Silurian Wufeng and Longmaxi Shale in the Sichuan Basin were studied to understand the genesis and diagenetic evolution of carbonate minerals and their effects on reservoir quality. The results of geochemical and petrological analyses show that calcite grains have a negative Ce anomaly indicating they formed in the oxidizing environment of seawater. The high carbonate mineral contents in the margin of basin indicate that calcite grains and cores of dolomite grains appear largely to be of detrital origin. The rhombic rims of dolomite grains and dolomite concretions with the $\delta^{13}C$ of −15.46‰ and the enrichment of middle rare earth elements were formed during the sulfate-driven anaerobic oxidation of methane. The calcite in radiolarian were related to the microbial sulfate reduction for the abundant anhedral pyrites and $\delta^{13}C$ value of −11.34‰. Calcite veins precipitated in the deep burial stage with homogenization temperature of the inclusions ranging from 146.70 °C to 182.90 °C. The pores in shale are mainly organic matter pores with pore size mainly in the range of 1–20 nm in diameter. Carbonate minerals influence the development of pores through offering storage space for organic matter. When calcite contents ranging from 10% to 20%, calcite grains and cement as rigid framework can preserve primary pores. Subsequently, the thermal cracking of liquid petroleum in primary pores will form organic matter pores. The radiolarian were mostly partially filled with calcite, which combining with microcrystalline quartz preserved a high storage capacity.

1. Introduction

The original sedimentary components of shale and their alterations during diagenesis are important factors in affecting the development and preservation of pores in shale gas reservoirs (Aplin and Macquaker, 2011; Loucks et al., 2012; Milliken et al., 2012; Milliken and Day-Stirrat, 2013; Macquaker et al., 2014; Yuan et al., 2021). Carbonate minerals contain information on the water column conditions, biology, climate and provenance, as well as conditions that lead to the growth, compositional changes and destruction during the burial. Consequently, the minerals contain a significant amount of information that can be used to understand the properties of sedimentary and diagenetic fluids to deduce original depositional conditions (Tucker, 1982; Derry et al., 1992; Jacobsen and Kaufman, 1999; Knauth and Kennedy, 2009).

Sedimentary carbonate minerals have three sources: physicochemically-related inorganic precipitation which are related to the calcium ion saturation, crystallization rate, magnesium-calcium ratio and salinity of seawater, biologically mediated mineralization which can increase pH values of the fluids through the metabolic processes of microorganisms and detrital transport through gravity flows, storm currents, and slumps (Reitner, 1993; Castanier et al., 1999; Reitner et al., 2015; Ries, 2004; Porter, 2007, 2010; Dupraz et al., 2009; Morad et al., 2010; Gallagher et al., 2012; Balthasar and Cusack, 2015). During diagenesis, microbial sulfate reduction (MSR), sulfate-driven anaerobic oxidation of methane (SD-AOM), the microbial

* Corresponding author. National Key Laboratory of Deep Oil and Gas, China University of Petroleum (East China), Qingdao, Shandong, 266580, China.
E-mail address: zhaojh@upc.edu.cn (J.-H. Zhao).

https://doi.org/10.1016/j.petsci.2023.08.012

methanogenesis of organic compounds and organic acids released by thermal evolution of organic matter can influence the precipitation of carbonate minerals (Berner et al., 1970; Curtis, 1980; Baker and Kastner, 1981; Compton, 1988; Cobbold et al., 2013; Wang et al., 2018). Exogenous calcium carbonate dissolved in migrating fluids may also play a role in sedimentation and diagenesis (Dutton, 2008). The calcite-precipitating fluids of calcite veins within the Wufeng and Longmaxi Formations were derived largely from their respective surrounding host-rock sources (Gao et al., 2019). The stratigraphic locus of precipitation migrated closer to highly alkaline sulfate-methane transition zone resulting in calcium carbonate precipitation in the barite-calcite-pyrite assemblages in the Longmaxi Formation (Zan et al., 2022).

The different precursors and origins of fine-grained carbonate sediments result in variable mineral compositions and sedimentary structures. This, in turn, can create differences in reservoir properties (Jarvie et al., 2007; Rickman et al., 2008; Slatt and O'Brien, 2011; Chalmers et al., 2012). In organic-rich shale reservoirs, carbonate minerals also have an important impact on the development, transformation and evolution of reservoir space. Early diagenetic carbonates are common in many organic-rich mudstones due to the oxidation and reduction reactions during shallow burial (Macquaker et al., 2007, 2014), and the distributions, sources and the timing of precipitation of carbonate cements frequently affect reservoir quality (Liu et al., 2014; Cui et al., 2017). The effect of carbonate mineral content on pore structure is also variable. For example, in the Alberta Belle Fourche Formation shale and Second White Specks Formation shale, the content of carbonate minerals is generally positively correlated with the abundance of micropores (< 2 nm) ($R^2 = 0.8$), while the dissolution of carbonate minerals in the Haynesville Shale can form a pore network with a good connectivity that is closely related to the occurrence of macropores (> 50 nm) (Chalmers et al., 2012; Hu et al., 2015; Furmann et al., 2016). The formation time of the dissolution pores in carbonate minerals has a controlling effect on shale gas enrichment in the Wufeng Formation and the Longmaxi Formation in the Sichuan Basin (Nie et al., 2019).

In recent years, shale gas exploration and development in China has made a breakthrough in marine shale in Sichuan Basin, and Fuling, Changning and other shale gas fields have been discovered successively (Zou et al., 2010; Zou et al., 2015; Ma and Xie, 2018). The organic-rich shale of the Silurian Longmaxi Formation in the Sichuan Basin is the principal exploration and production interval for shale gas in China. The enrichment degree of natural gas in highly mature shale is directly controlled by pore structure (Jarvie et al., 2007; Zou et al., 2015; Chen et al., 2019). Carbonate minerals have an important impact on pore structure in organic-rich shale reservoirs (Zhou et al., 2022; Zheng et al., 2022). However, the influence of carbonate minerals on the shale reservoir quality of Longmaxi Formation has been less studied by predecessors. The purpose of this study, then, is to elucidate the genesis and diagenetic evolution of carbonate minerals and the effect of sedimentary and diagenetic carbonate minerals on pore development in reservoirs. In this study, carbonate minerals in marine shale of the Wufeng and Longmaxi Shale in the Sichuan Basin are classified based on macroscopic and microscopic characteristics of carbonate minerals. The origin of different types of carbonate minerals are determined through analyses such as inorganic carbon and oxygen isotopic ratios, rare earth elements and yttrium concentrations. In addition, the pore structure of these reservoirs is characterized by scanning electron microscope (SEM), mercury intrusion porosimetry (MIP) and low-pressure nitrogen sorption isotherm experiments.

2. Geological setting

The Sichuan Basin and its surrounding areas are a part of the Yangtze block, located in the west of Yangtze paraplatform. It is a superimposed basin developed on the Upper Yangtze Craton. The Caledonian Orogeny reached its maximum intensity from the Late Ordovician to the Early Silurian period, which compressed the Upper Yangtze Block. This compression resulted in the formation of the Chuanzhong Uplift in the northwestern Yangtze Block, the Qianzhong Uplift in the southern Yangtze Block and the Xuefeng Uplift in the southeastern Yangtze Block (Fig. 1) (Zou et al., 2015; Ma and Xie, 2018). The Sichuan Basin and its adjacent areas consequently consisted of three uplifts and one depression at this time, while a semi-closed bay opening to the north appeared in the Middle-Upper Yangtze region (Fig. 1) (Wang et al., 2014a).

Two large-scale global transgressions occurred in the Late Ordovician and the Early Silurian during which timed the deposition of the Wufeng and Longmaxi Shale (Su et al., 2007). Relatively low energy and anoxic conditions resulted in the deposition of thick organic-rich shales in the southern Sichuan Basin (Zhao et al., 2016a). They have a rather homogeneous, detrital-sourced, and coarser-grained component vertically (Zhao et al., 2016b). The tectonic movements and transgressions also led to thin layers of siliceous shale being deposited in the late Ordovician (Chen et al., 2000). This siliceous shale is widely distributed at a thickness ranging from a few to tens of meters with rich radiolarian (Fig. 2) (Su et al., 2007; Zhao et al., 2016b).

3. Samples and methods

The Wufeng and Longmaxi Shale was studied on core samples acquired from three wells and regions (Y1 in Luzhou area, N1 in Changning area and W1 in Weiyuan area) in the Sichuan Basin (Fig. 1). A total of 121 samples were collected for thin section identification and bulk rock X-ray diffraction (XRD) analyses (54 samples in Y1; 36 samples in N1; 31 samples in W1). Among them, bulk rock inorganic carbon and oxygen isotope tests were carried out on 28 samples (Y1-1 – Y1-3; N1-1 – N1-16; W1-1 – W1-9); one sample was subjected to fluid inclusion analysis (N1-1); seven samples were subjected to analysis of rare earth elements and yttrium concentrations (REE + Y) (Y1-1 – Y1-3; N1-3 – N1-5, N1-9); 16 samples were selected to carry out SEM imaging and MIP tests (Y1-4 – Y1-9; W1-3, W1-4, W1-6, W1-9 – W1-15); and 20 samples were subjected to total organic carbon content (TOC) analysis and low-pressure nitrogen physisorption experiments (Y1-3 – Y1-10; W1-3, W1-4, W1-6, W1-9 – W1-16).

Thin sections were observed using a Leica DM4P microscope under transmitted polarized light to identify the carbonate minerals. A Zeiss Crossbeam 550 SEM was used to observe microscopic minerals and pores, with Energy Disperse Spectroscopy (EDS) used for mineral characterization. The samples for SEM imaging were polished with an argon ion mill in order to create an extremely flat, artifact-free surface. A carbon film was coated on the surface of samples to increase the electrical conductivity.

The mineralogical composition of bulk samples, after the samples being ground to less than 200 mesh powder, was determined by XRD to pinpoint the variation of carbonate mineral content in different wells. The structure of the shale samples was analyzed using D8 A25 X-ray diffractometer. The voltage was set to 45 kV and current to 40 mA, and continuous scanning was performed at 24–26 °C with the minimum diffraction angle of 2°. The TOC was analyzed with a LECO CS 744 carbon/sulfur analyzer, after samples (80–100 mesh powder) were treated by adding hydrochloric acid

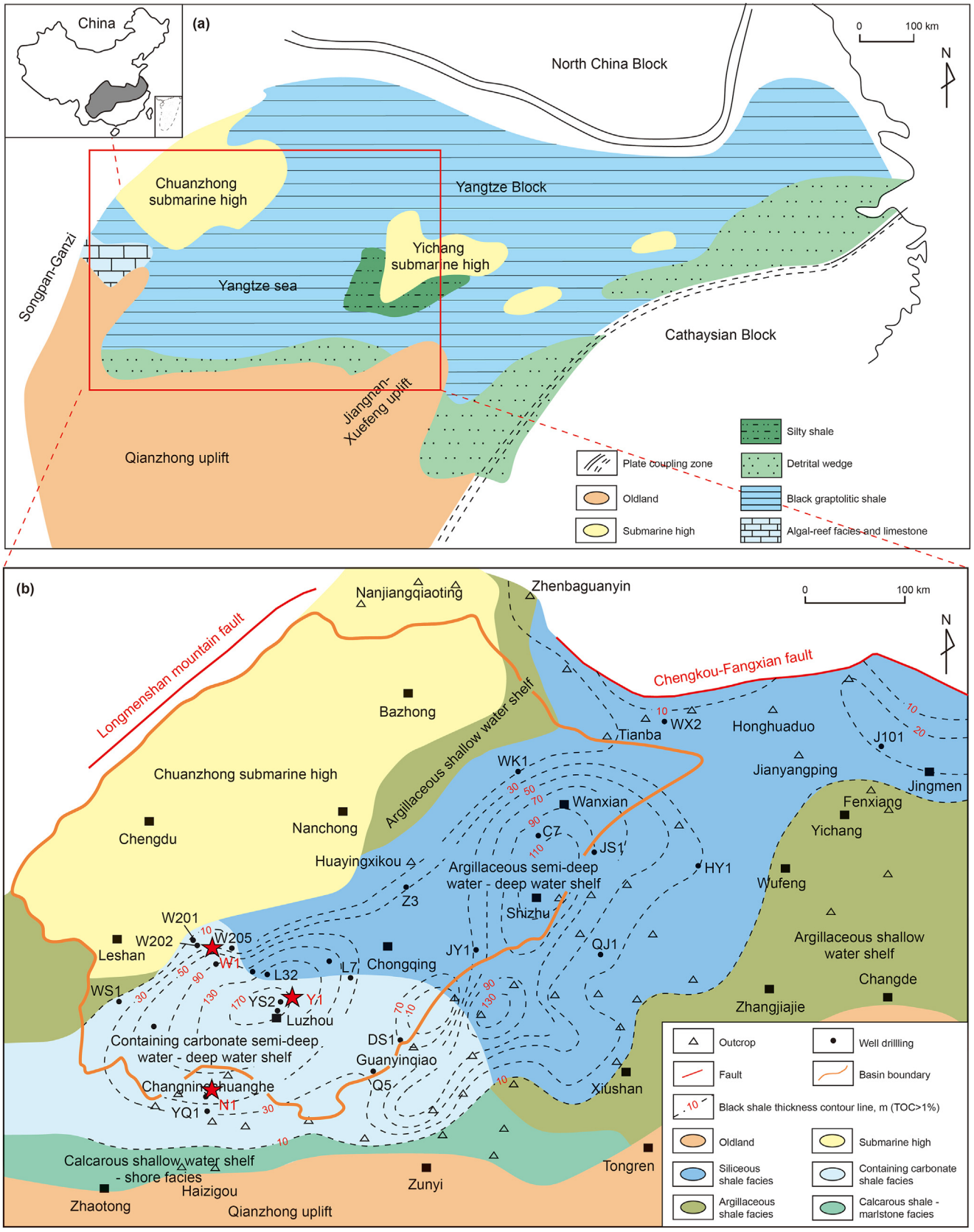

Fig. 1. (a) Paleolithofacies map of the Early Silurian in the Yangtze region (Zhao et al., 2016b); (b) Sedimentary facies map of the early sedimentary Longmaxi Shale in the Sichuan Basin and adjacent areas (Zou et al., 2015).

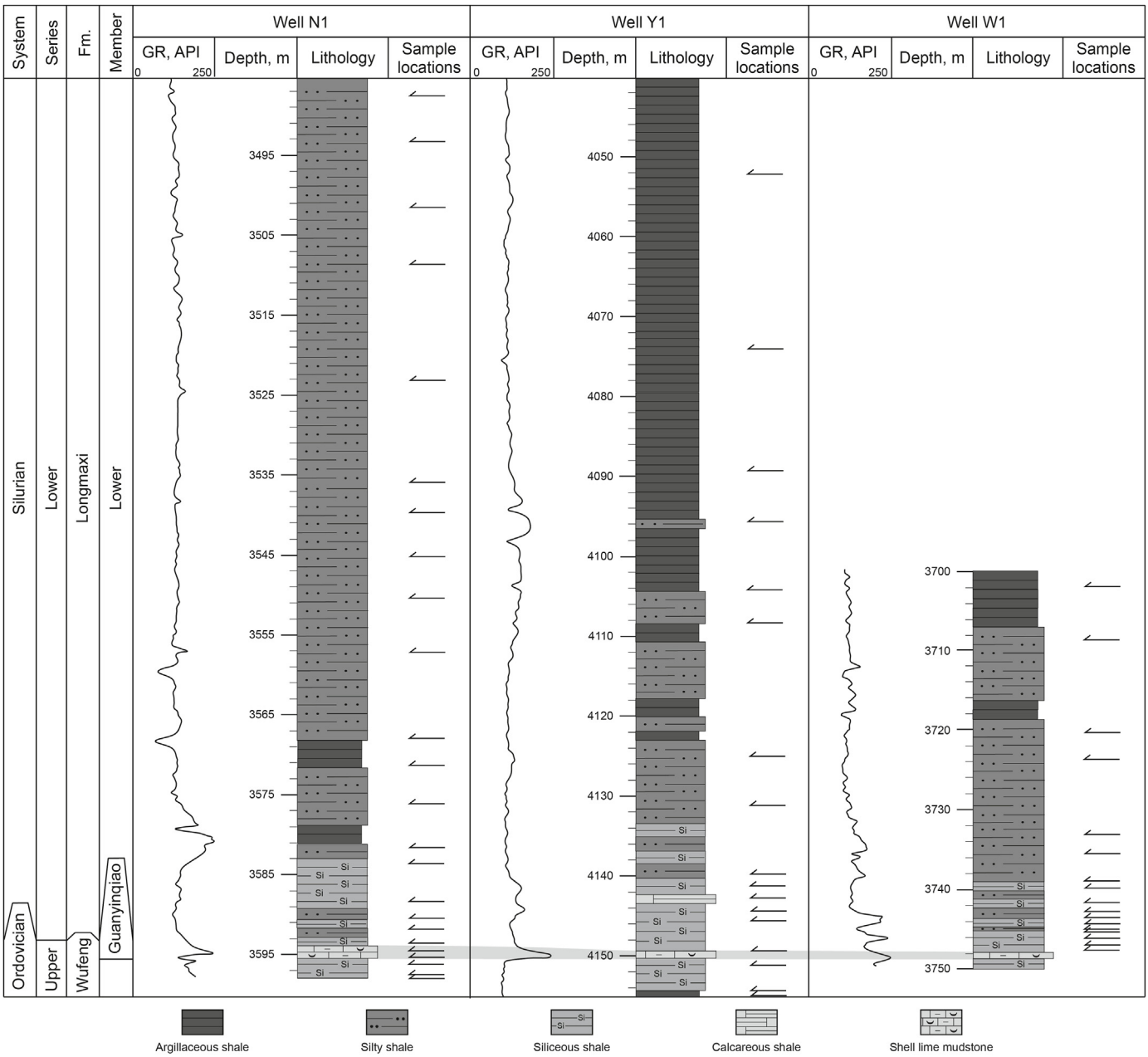

Fig. 2. Stratigraphic column of the study area.

(HCl: water = 1:7) for several times to remove inorganic carbon, adding water for several times to remove acid and drying at 120 °C for 2 h. The fluid inclusion analysis was completed on the Linkam-THMSG600 heating and freezing stage with a heating rate of 10 °C/min at temperatures less than 100 °C and a rate of 2 °C/min at temperatures exceeding 100 °C.

The carbon and oxygen isotopes of bulk rock were measured on the MAT253 gas stable isotope mass spectrometer using samples ground to under 200 mesh. Analyses were reported relative to Vienna Peedee Belemnite (V-PDB) with an analytical uncertainty of less than ± 0.16‰ (1σ). The REE + Y analyses were performed using inductively coupled plasma mass spectrometry (ICP-MS) using an Agilent 7700e instrument for ground samples. One hundred milligrams of sample were digested with 1 mL of HF and 0.5 mL of HNO_3 in PTFE-lined stainless steel bombs heated to 200 °C for 12 h. Insoluble residues were dissolved using 6 mL of 40% v/v HNO_3 heated to 140 °C for 3 h (Qi and Gregoire, 2000). The results were referenced to PAAS.

The MIP analyses were performed with a Micromiritics AutoPore IV 9520 mercury intrusion porosimeter, with pressure ranging from 0.034 MPa to 413 MPa (1 MPa = 145 psi). The corresponding pore-throat diameters were calculated and corrected by the modified Washburn equation ranging from 50 μm to 2.8 nm (Washburn, 1921; Wang et al., 2016). The low-pressure nitrogen physisorption experiments were carried out on a Micromeritics ASAP 2460 apparatus, which can measure pore diameters ranging from 1.2 to 300 nm. The pore size distribution was obtained using the density functional theory (DFT) methods (Seaton and Walton, 1989; Lastoskie et al., 1993).

4. Results

4.1. Types and characteristics of carbonate minerals

4.1.1. Calcite and dolomite grains

Carbonate mineral grains are colorless and transparent under plane polarized light, and have advanced white interference color under crossed polarized light. There are two grain size ranges: micrite grade (< 5 m) and silt grade (5–100 m) which is further divided into coarse silt grade (50–100 m) and fine silt grade (5–50 m). Carbonate mineral grains can be floating in the shale matrix, and exist as lenticular and laminated aggregates (Fig. 3).

Calcite grains are generally anhedral, and are commonly near-spherical, near-cylindrical, and other irregular forms (Fig. 4a–c). Subhedral, smooth nanoscale calcite aggregates are also observed (Fig. 4d). Dolomite grains are euhedral-subhedral rhombohedral (Fig. 4e and f). EDS data demonstrate that the dolomite grains consist of rhombic rims of ankerite and irregularly shaped core zones of non-ferroan dolomite (Fig. 4g). Differential compaction can be observed between the boundaries of calcite and dolomite grains and surrounding minerals (Fig. 4g and h). A numbers of dolomite grains have the characteristics of foggy center and bright edge with rough core zones, as well as clean and bright rims under optical microscope (Fig. 3g and h).

4.1.2. Calcite in interparticle pores

In shales with a high content of terrigenous minerals (like quartz and feldspar), there are often no clear boundaries between calcite and aggregated or lamellar siliciclastic mineral grains. In contrast to calcite and dolomite grains discussed above, calcite in interparticle pores do not have regular mineral morphology (Fig. 5). Instead, they are distributed around terrigenous siliciclastic minerals in various irregular forms, filling the pores between felsic minerals.

4.1.3. Calcite in radiolarian

In the lower siliceous shale, although many radiolarian are broken into fragments, some are well preserved and can reach a size of 300 m (Fig. 6). Since the radiolarian are originally siliceous organisms, their cavities are often filled with microcrystalline quartz, which is due to the dissolution and reprecipitation of the tests of siliceous organisms (Schieber et al., 2000; Zhao and Jin, 2021).

However, in many radiolarian fragments, incomplete rhombic calcite occur in radiolarian (Fig. 6a and b). Calcite also appears as curved strips around the cavity in a few radiolarian fragments (Fig. 6c and d). When radiolarian are almost completely filled with irregular calcite grains, the calcite grains in the center of radiolarian are larger than these at the edges of radiolarian (Fig. 6e and f). Furthermore, the anhedral and subhedral pyrite grains are abundant with the largest diameter reaching 30 m (Fig. 6g and h). The content of pyrite in the sample which is completely filled with calcite can reach 13.30%.

4.1.4. Calcareous shells and shell fragments

An abundance of shell occurs in the Guanyinqiao section at the top of the Wufeng Shale, including brachiopods and lamellibranchias. Some shells are relatively well preserved with sizes ranging from dozens of micrometers to hundreds of micrometers, and even up to a few centimeters. The shells are always deposited parallel to the bedding planes (Fig. 7a and b). In some of the shell fossils, the calcareous periphery has been replaced by quartz, while the interiors of the shells are frequently calcite (Fig. 7c and d). Most shells are almost completely calcite (Fig. 7e and f) which retain their original shapes and structures.

4.1.5. Calcite veins

There are bedding-parallel veins of fibrous crystals (referred to as “beef” by Cobbold et al., 2013) in the Longmaxi Shale. Most of calcite veins are about 50–200 m in width and less than 2 cm in length (Fig. 8a and b). Calcite veins are always lenticular and arcuate. Discontinuous organic matter may occur in them. Veins can also appear as the superposition of multiple lenticular fibrous calcite veins with a width reaching up to 5 mm (Fig. 8c and d). Each lenticular calcite vein has its own median line, which is basically parallel to the wall rocks on both sides of the calcite vein, and develops asymmetrically (i.e., is closer to one side of the vein). The median line shows a dark brown color in transmitted light (Fig. 8c and d). The calcite in the veins is fibrous and the crystals are parallel to one other, and almost perpendicular to the surrounding rocks. Solid inclusions of wall-rock enclosed within the fibers are a distinctive feature of beefs (Wang et al., 2018). The composition of solid inclusions in calcite veins is consistent with the surrounding rock, and the shapes or trails of solid inclusions rang from parabolic to sinusoidal (Wang et al., 2018; Luan et al., 2019) (Fig. 8c and d). Calcite veins perpendicular to the stratification direction also exist. They have a lateral width of about 50 m, curved shape, and jagged edge (Fig. 8e and f).

4.1.6. Dolomite concretions

Dolomite concretions can be observed in the upper interval of the Longmaxi Shale (Sample Y1-1 at 4072 m in Well Y1) with the largest concretion being more than 10 cm in diameter (Fig. 9a and b). Many discontinuous thin layers of clay minerals can be observed in the dolomite concretions using optical microscope. The dolomite is densely distributed and has no obvious crystal morphology (Fig. 9c and d). Under SEM observations, the nodular dolomite is very densely packed and there is also a significant amount of clay minerals (Fig. 9e). Some euhedral and framboidal pyrite also occurs in the dolomite concretions (Fig. 9f).

4.2. Distributions of carbonate minerals

The Wufeng and Longmaxi Shale contain a variety of lithofacies that can be identified on the basis of sources of the grains, grain size, fabric, biota, sedimentary structures and composition (Yuan et al., 2023). In this study, the following five general lithofacies are recognized based on mineral composition, mineral origin and diagenesis. Argillaceous shale is characterized by a high content of clay minerals (> 50%). Calcareous shale has high calcite or dolomite contents (> 50%). Quartz in silty shale is mainly detrital in origin (> 45%), while siliceous shale has a high content of authigenic microcrystalline quartz in thin section and SEM (> 45%). Shell lime mudstone contains amounts of calcareous shells.

The content of carbonate minerals in Well Y1 samples is generally low expect for the calcareous shale. While the contents of carbonates in samples from Well N1 and Well W1 are generally higher (Table 1). The carbonate generally occurs as calcite and dolomite grains and calcite veins in argillaceous shale with an average calcite content of 1.89% and dolomite content of 1.88% in Well Y1, 10.38% and 10.39% in Well N1, 1.60% and 2.40% in Well W1. The radiolarian which are completely filled with calcite are the carbonate mineral type in calcareous shale with a calcite content of 70.80% and dolomite content of 1.30%. The silty shale commonly have calcite and dolomite grains, calcite cements and veins with an average calcite content of 5.65% and dolomite content of 4.72% in Well Y1, 17.48% and 10.02% in Well N1, 15.36% and 9.57% in Well W1. The carbonate generally occurs as calcite in radiolarian and calcite and dolomite grains in siliceous shale with an average calcite content of 3.57% and dolomite content of 4.49% in Well Y1, 15.98% and 10.23% in Well N1, 5.12% and 4.28% in Well W1 (Table 1, Fig. 10).

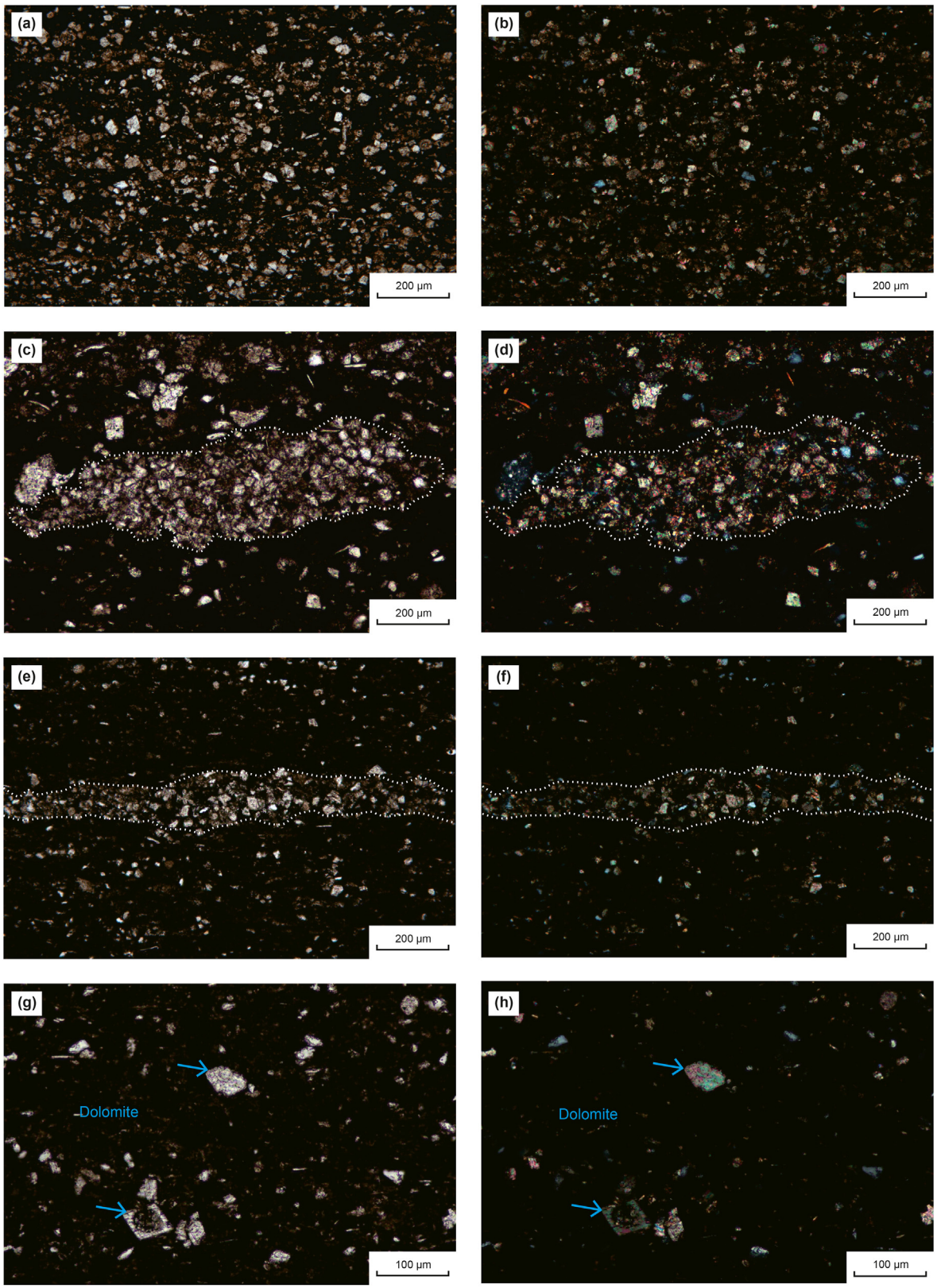

Fig. 3. Optical microscope of carbonate mineral grains: (a–b) Plane and crossed polarized light of floating carbonate mineral grains (Sample W1-17); (c–d) Plane and crossed polarized light of lenticular aggregates of carbonate mineral grains (Sample N1-17); (e–f) Plane and crossed polarized light of lamellar carbonate mineral grains (Sample Y1-11); (g–h) Plane and crossed polarized light of dolomite grains with characteristic foggy centers and bright edges (Sample Y1-16).

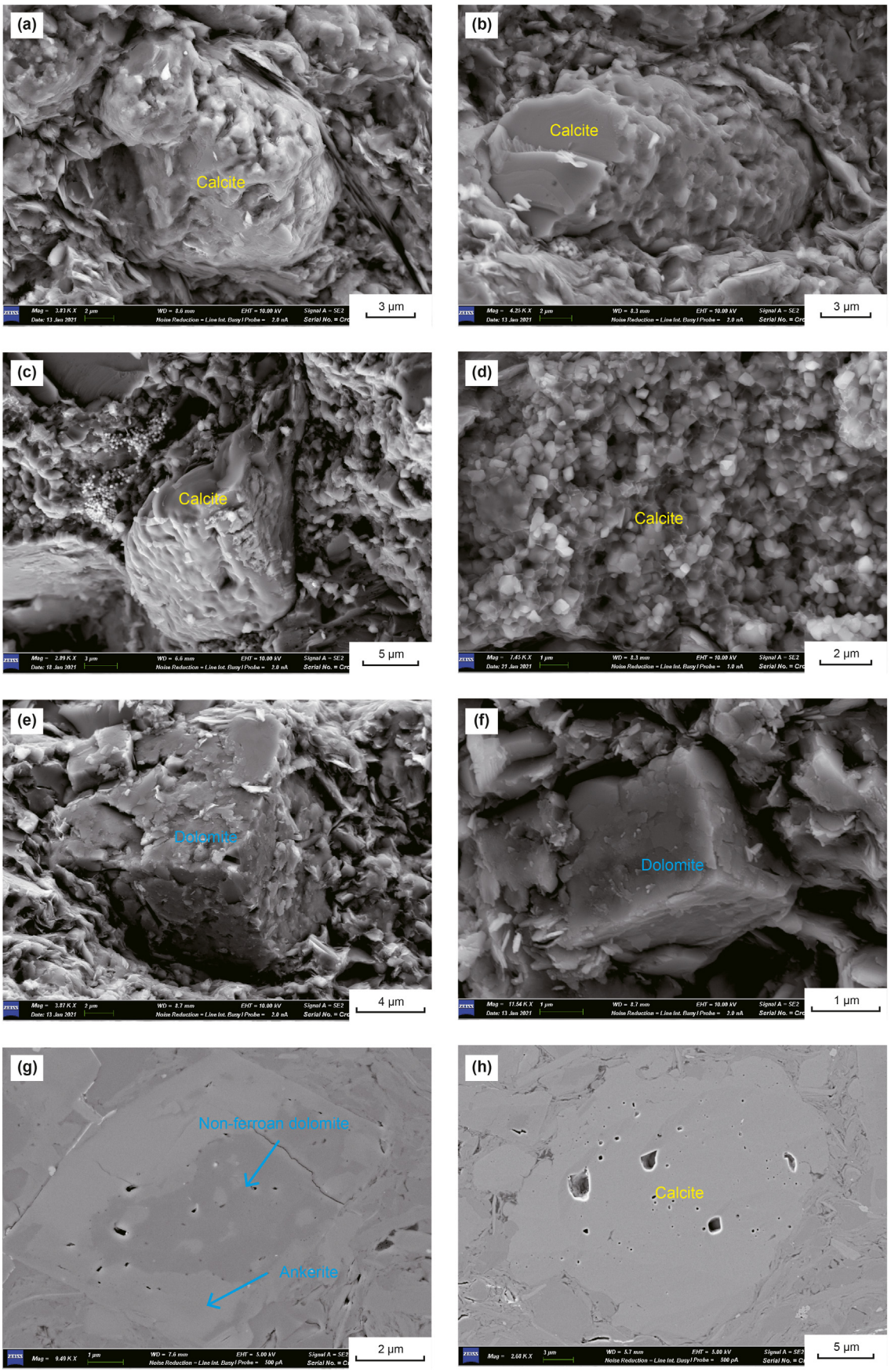
(a)
Calcite
3 μm
(b)
Calcite
3 μm
(c)
Calcite
5 μm
(d)
Calcite
2 μm
(e)
Dolomite
4 μm
(f)
Dolomite
1 μm
(g)
Non-ferroan dolomite
Ankerite
2 μm
(h)
Calcite
5 μm

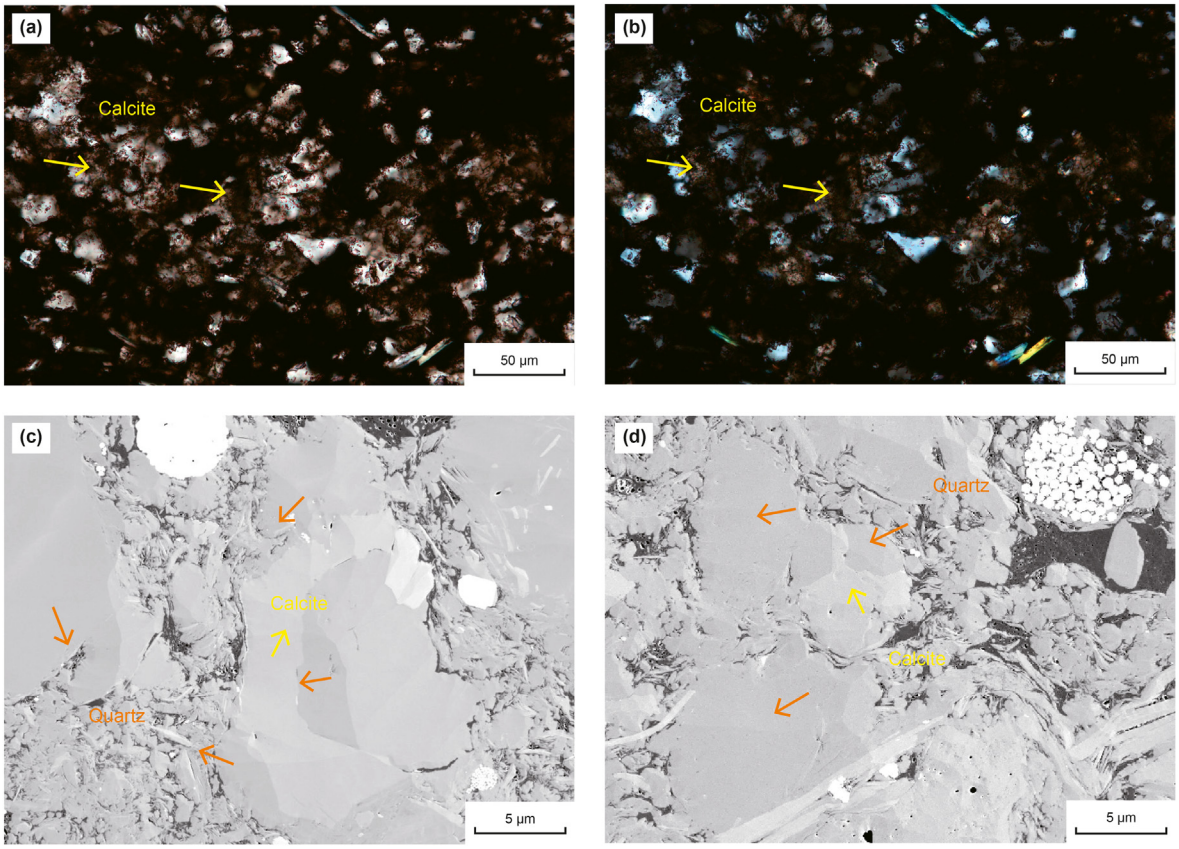

Fig. 5. Calcite filling pores in siliciclastic minerals: (a–b) Plane and crossed polarized light of calcite minerals between siliciclastic mineral grains (Sample W1-19); (c–d) SE images of calcite minerals between siliciclastic mineral grains (Sample W1-19).

Calcareous shell fragments are observed in the Wufeng Shale (Fig. 10). Dolomite concretions are only observed in the upper interval of the Longmaxi Shale in Well Y1 (Fig. 10).

4.3. Carbon and oxygen isotopic ratios

Thin section observations and SEM images suggest that calcite and dolomite grains are the main calcite minerals in most samples (except for samples of calcite in radiolarian, dolomite concretions and calcite veins). In addition, caicite cement in samples is rare. Therefore, the samples with high calcite and low dolomite contents from the XRD tests represent calcite grains. They have a $\delta^{13}C$ ranging from −1.91‰ to 0.54‰, and a $\delta^{18}O$ ranging from −11.47‰ to −10.09‰. The samples with high dolomite but low calcite contents represent dolomite grains. They have a $\delta^{13}C$ ranging from −5.74‰ to 0.45‰, and a $\delta^{18}O$ ranging from −10.57‰ to −3.71‰. The calcite in radiolarian have a $\delta^{13}C$ of −11.34‰ and a $\delta^{18}O$ of −13.52‰. The $\delta^{13}C$ of dolomite concretions is −15.46‰, and the $\delta^{18}O$ is −10.79‰. Testing the powder of calcite veins obtained by micro-drilling, $\delta^{13}C$ values of two calcite veins are −5.44‰ and −3.81‰, and $\delta^{18}O$ values are −12.12‰ and −10.58‰ (Fig. 11, Table 2).

4.4. Rare earth elements and yttrium

The distributions of REE + Y of calcite grains are characterized by the depletion of light rare earth elements (LREE) relative to middle rare earth elements (MREE) and heavy rare earth elements (HREE) (Fig. 12a). The Y/Ho radios of calcite grains which range from 1.42 to 1.62 indicate significant positive Y anomalies (Table 3). The La/La* and Gd/Gd* radios range from 1.19 to 1.30 and 1.18 to 1.23, they suggest the weakly positive La and Gd anomalies (Table 3). The Ce/Ce* radios range from 0.76 to 0.78, and the calcite grains have negative Ce anomalies (Table 3). The REE + Y pattern of calcite in radiolarian fully filled with calcite sample is characterized by a LREE depletion (Fig. 12b) The Y/Ho, La/La* and Eu/Eu* ratios of calcite in radiolarian are 1.65, 2.04 and 2.02, which indicate significant positive Y anomaly, positive La anomaly, and positive Eu anomaly (Table 3). Dolomite grains have no obvious element positive and negative anomalies (Fig. 12c), and dolomite concretions are characterized by MREE enrichment and LREE and HREE depletion (Fig. 12d).

4.5. Fluid inclusions

Large fluid inclusions are difficult to find in samples of calcite and dolomite grains, calcite in radiolarian, dolomite concretions and calcite veins. They can only be seen in calcite veins with large

Fig. 4. SEM microscope of carbonate mineral grains: (a–b) Secondary electron (SE) images of near-spherical and near-cylindrical calcite grain (Sample Y1-12); (c) SE image of irregular calcite grain (Sample Y1-13); (d) SE image of nanoscale calcite grain (Sample Y1-8); (e) SE image of silt grade dolomite grain (Sample Y1-14); (f) SE image of micrite dolomite grain (Sample Y1-14); (g) SE image of rhombic rims of ankerite and irregularly shaped core zones of non-ferroan dolomite (Sample Y1-14); (h) SE image of different compaction between boundary of calcite grain and surrounding minerals (Sample Y1-15).

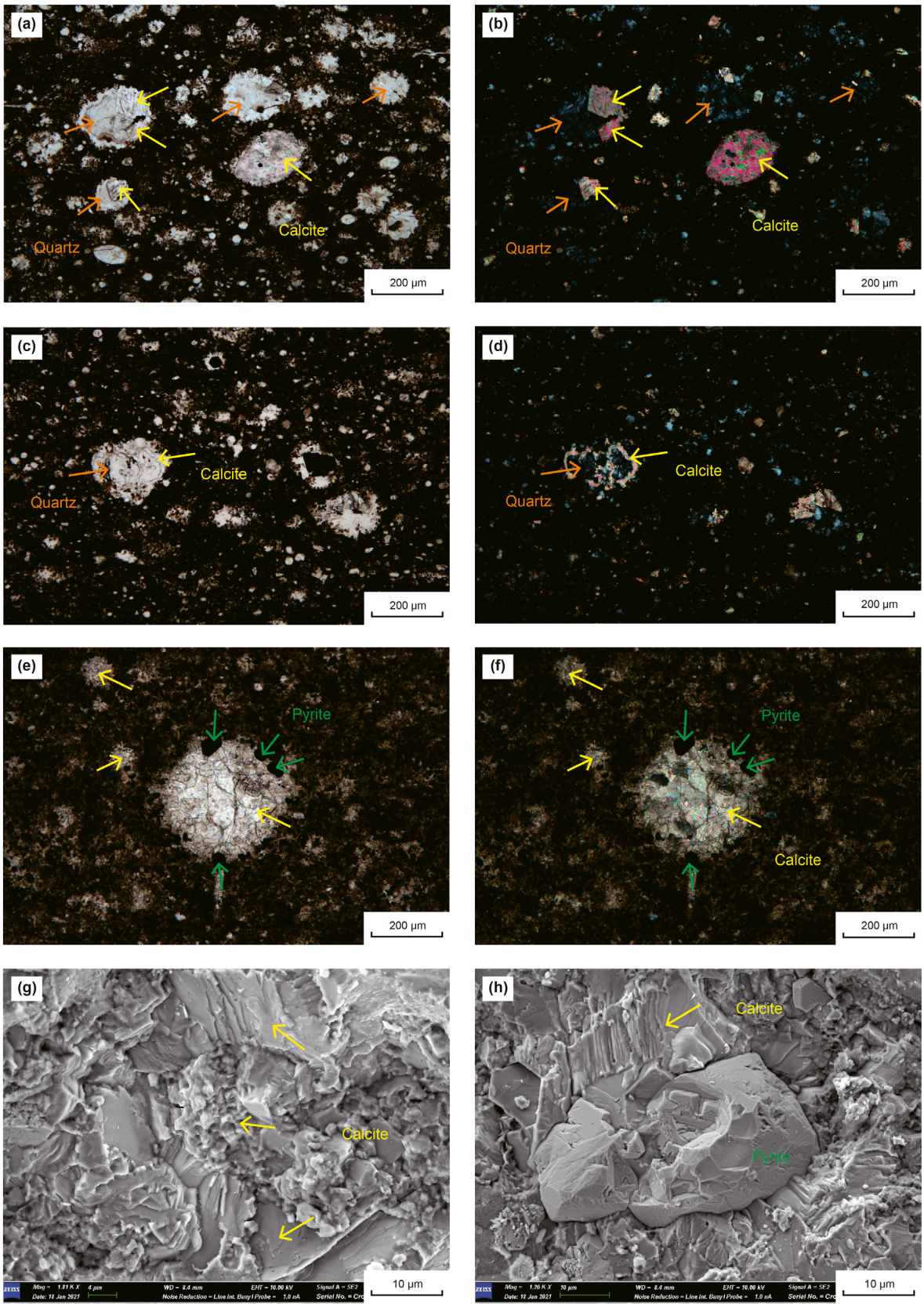

Fig. 6. Occurrences of calcite and pyrite in radiolarian: (a–b) Plane and crossed polarized light of incomplete rhombic calcite in radiolarian (Sample W1-12); (c–d) Plane and crossed polarized light of calcite with curved strips around cavity in radiolarian (Sample W1-20); (e–f) Plane and crossed polarized light of radiolarian completely filled with calcite (Sample Y1-3); (g–h) SEM images of calcite and pyrite in radiolarian (Sample Y1-3).

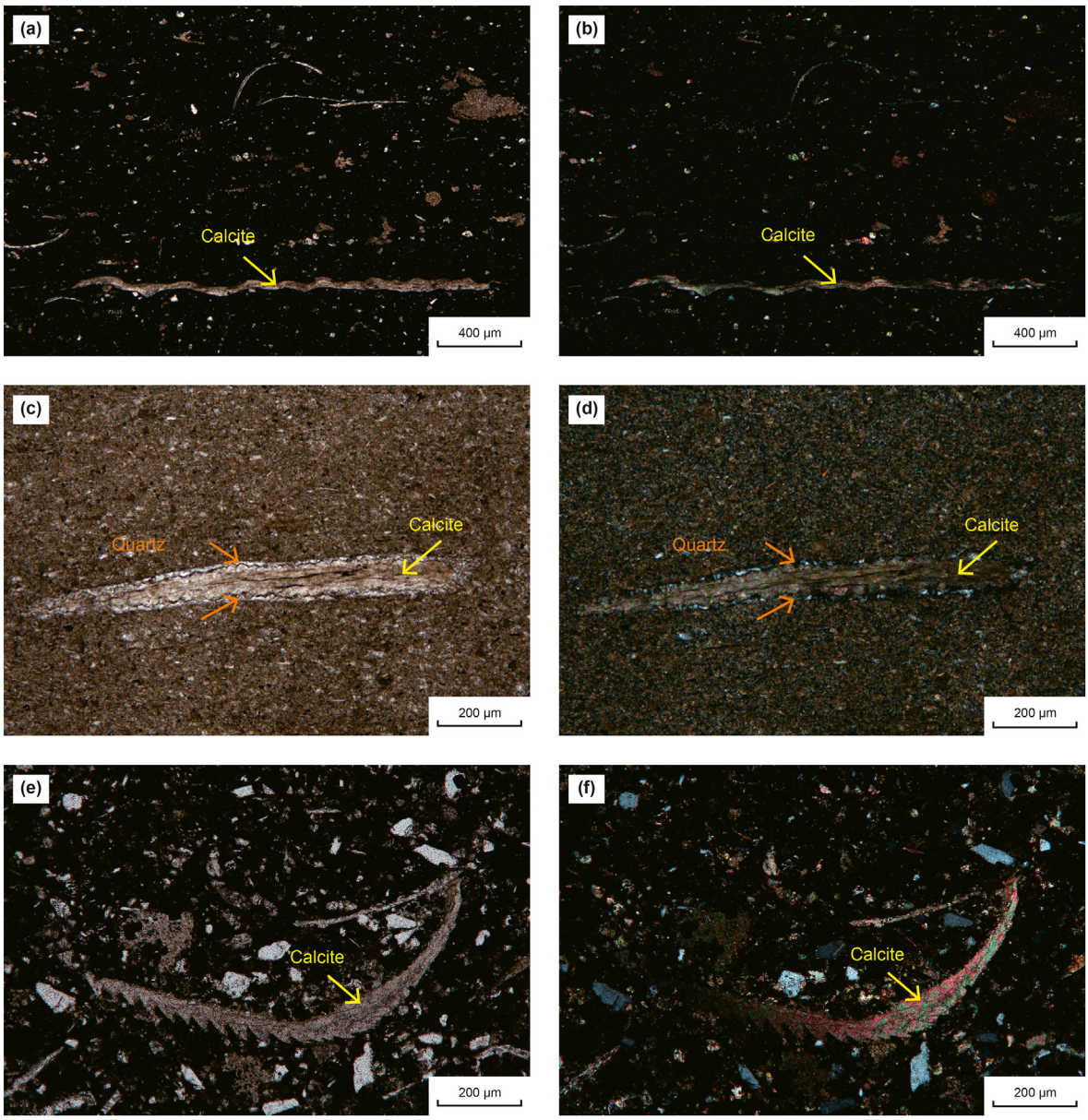

Fig. 7. Calcite in biological shell: (a–b) Plane and crossed polarized light of parallelly arranged shells (Sample W1-9); (c–d) Plane and crossed polarized light of calcite in the interiors of shells (Sample Y1-7); (e–f) Plane and crossed polarized light of shells completely recrystallized by calcite (Sample N1-16).

thickness (>5 mm aperture) (Fig. 13). Therefore, only Sample N1-1 has the gas-liquid two-phase brine inclusions. The homogenization temperatures measurement of the gas-liquid two-phase brine inclusions in the calcite veins range from 146.70 °C to 182.90 °C (Table 4).

4.6. Reservoir physical properties

4.6.1. Pore types

The predecessors have done a lot of research on the pore types of the Longmaxi Shale. Organic pores, mineral matrix pores, lamination fractures and micro-fractures are common in the first member of the Longmaxi Shale. The Longmaxi Shale is dominated by organic pores with good pore connectivity, making it the most effective storage space for shale gas (Guo and Zhang, 2014; Wang et al., 2014b; Zou et al., 2015; Cai et al., 2020). Our research is consistent with previous conclusions.

The types of pores and fractures developed in the first member of the Wufeng and Longmaxi Shale in the southern Sichuan Basin include intergranular pores between microcrystalline quartz and calcite grains, calcite grain boundary seams and intragranular pores within clay mineral, framboidal pyrite and calcite grains (Fig. 14a–e). While pores in calcite grains are mostly quadrilateral with clear boundaries, which may be inclusions generated during mineral formation (Fig. 14e). Organic matters pores are often found in mineral matrix pores between carbonate minerals, siliciclastic minerals and clay minerals, and between microcrystalline quartz (Fig. 14f–g). Microfractures in the shale matrix are common (Fig. 14h).

4.6.2. Pore structure

MIP can characterize the macropore (> 50 nm) distribution characteristics of shale and low-pressure nitrogen physisorption characterizes the mesopore (2–50 nm) distribution characteristics

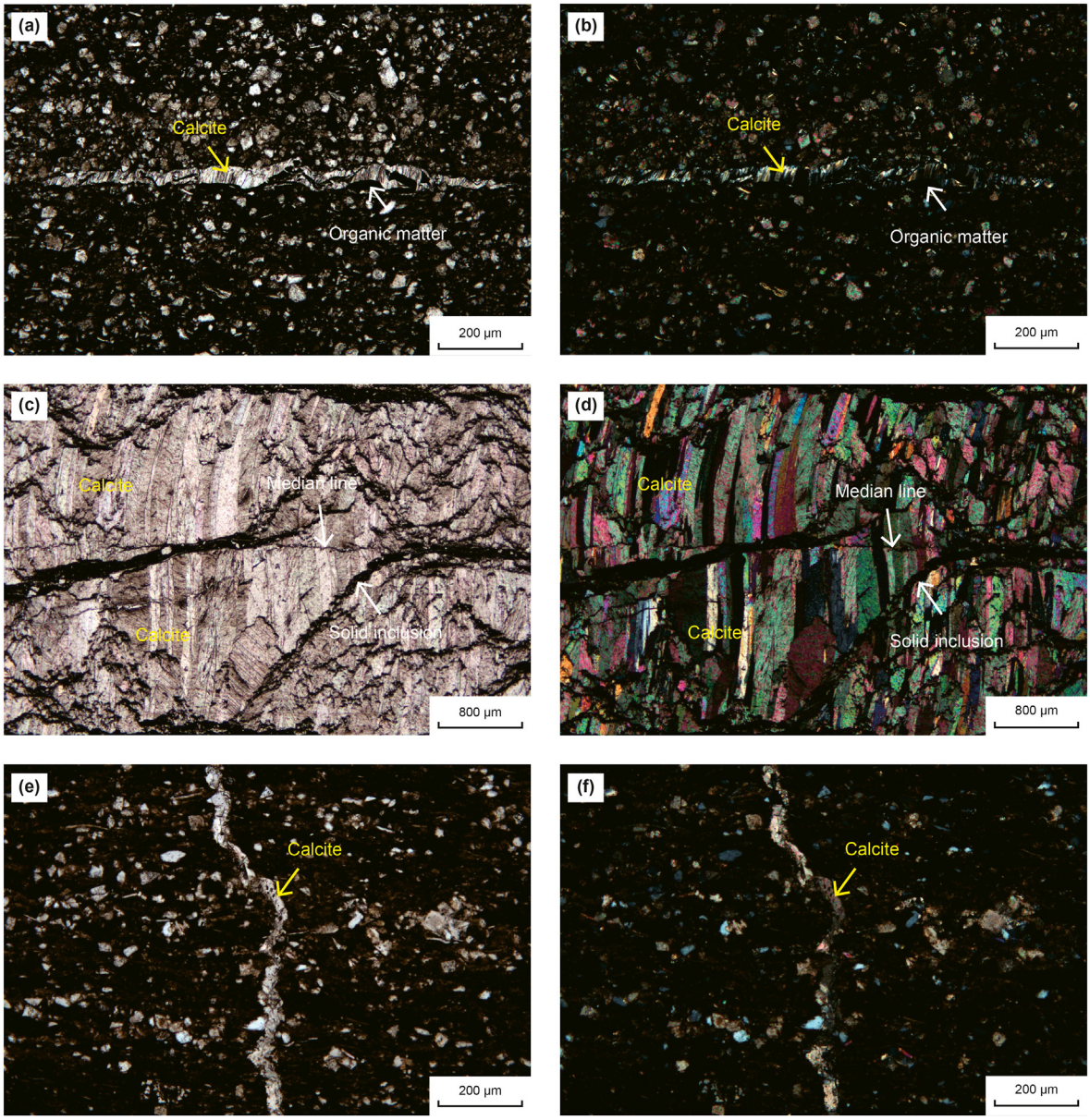

Fig. 8. Characteristics of calcite veins: (a–b) Plane and crossed polarized light of fibrous calcite veins (Sample N1-18); (c–d) Plane and crossed polarized light of the superposition of multiple lenticular fibrous calcite veins (Sample N1-1); (e–f) Plane and crossed polarized light of calcite veins vertical to the stratification direction (Sample W1-18).

of shale. Combining the advantages of these two testing methods, we can obtain more comprehensive pore structure information of different scales. The MIP data show that the total pore volume in Well Y1 samples is low, with an average porosity of 1.26%. In contrast, the total pore volume in Well W1 samples is higher with an average porosity of 2.63% (Table 5). The pore throat diameters of samples in the two wells are mainly in the range of 3–20 nm (Fig. 15). The DFT model of low-pressure nitrogen physisorption can be used to obtain the pore size distribution (Seaton and Walton, 1989; Lastoskie et al., 1993), which are principally in the range of 1–20 nm. The pore volume maxima occur at pore diameters of 1.2 nm, 1.6 nm and 3 nm, while a weaker positive peak appears at a pore diameter of 9 nm (Fig. 16).

Samples with different calcite and dolomite content have differences in the porosity and pore volume (Figs. 15–16, Table 6). Samples with calcite contents < 10% and dolomite contents < 10% have an average porosity of 0.93% in Well Y1, 2.34% in Well W1, and an average pore volume of 0.0102 cm^3/g in Well Y1, 0.0149 cm^3/g in Well W1 (Table 6). When 10% < calcite contents < 20%, and dolomite contents < 10%, samples have a higher average porosity of 1.92% in Well Y1, 4.22% in Well W1, and an average pore volume of 0.0158 cm^3/g in Well Y1, 0.0226 cm^3/g in Well W1 (Table 6). If 10% < calcite contents < 20% and dolomite contents >10%, samples have an average porosity of 2.93% and an average pore volume of 0.0181 cm^3/g (Table 6). For cases of calcite contents > 20% and dolomite contents < 10%, samples have an average porosity of 2.23%, and an average pore volume of 0.0155 cm^3/g (Table 6).

When the radiolarian are completely filled with calcite in Sample Y-3 (Fig. 6e–h), sample have a pore volume of 0.0155 cm^3/g (Fig. 17, Table 5). When the radiolarian are partly filled with calcite in Sample Y-10 and W-16 (Fig. 6a-d), sample have an average pore volume of 0.0155 cm^3/g (Fig. 17, Table 5).

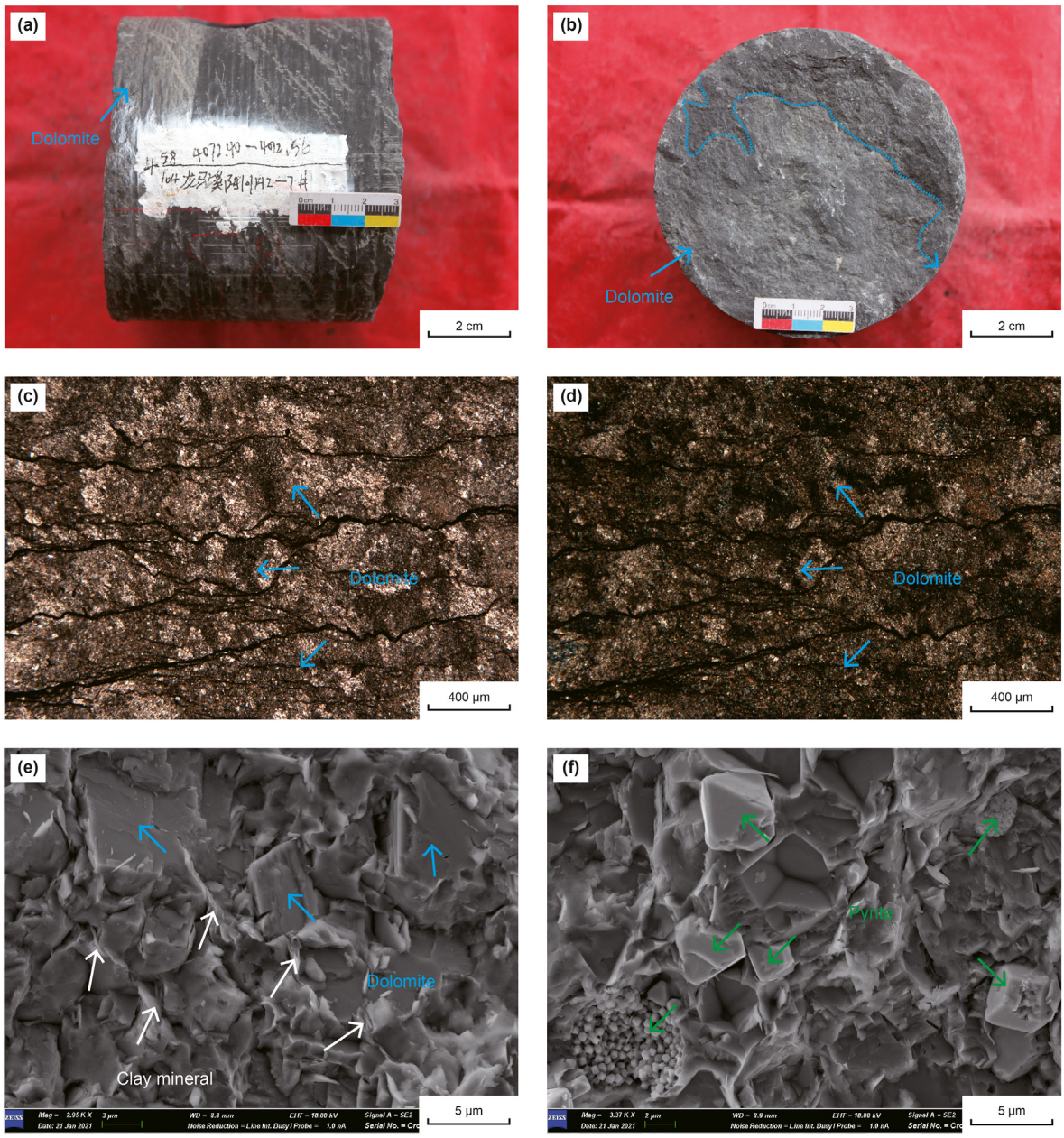

Fig. 9. Characteristics of dolomite concretions: (a–b) Plane and crossed polarized light of dolomite concretions in hand specimen, (Sample Y1-1); (c–d) Plane and crossed polarized light of transverse, curved, discontinuous thin layers of clay minerals in dolomite concretions, (Sample Y1-1); (e) SEM image of a large number of clay minerals distributed in the accumulated dolomite (Sample Y1-1); (f) SEM image of euhedral pyrite and framboidal pyrite (Sample Y1-1).

Table 1
Average calcite and dolomite content in lithofacies.

Lithofacies	Mineral type	Average content in wells, %		
		Y1	N1	W1
Argillaceous shale	Calcite	1.89	10.38	1.60
	Dolomite	1.88	10.39	2.40
Calcareous shale	Calcite	70.80		
	Dolomite	1.30		
Silty shale	Calcite	5.65	17.48	15.36
	Dolomite	4.72	10.02	9.57
Siliceous shale	Calcite	3.57	15.98	5.12
	Dolomite	4.49	10.23	4.28

5. Discussion

5.1. Genesis and diagenesis of carbonate minerals

5.1.1. Calcite grains

During the Silurian (440 to 418 Ma), the Mg^{2+}/Ca^{2+} ratios were < 2.3, while calcite was the dominant nonskeletal carbonate (Lowenstein, 2001). The Wufeng and Longmaxi Shale was deposited in a semi-deep to deep shelf environment (Zou et al., 2015). The occurrences of laminar and lenticular minerals and the input of terrestrial mineral grains indicate that the shale deposition was affected by various hydrodynamic actions such as submarine currents and traction flows. Consequently, it was difficult to form silt-sized calcite grains during the shallow burial of seabed sediments

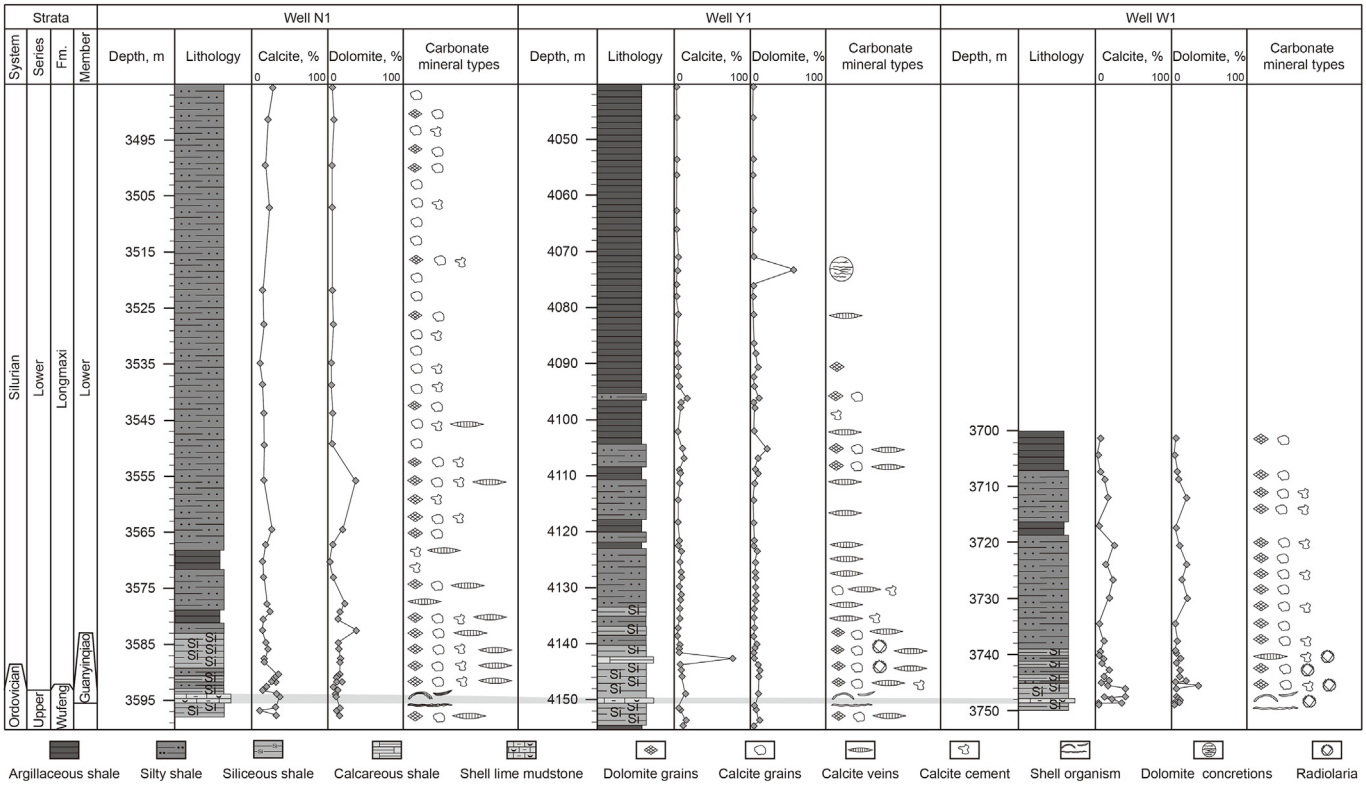

Fig. 10. Occurrences of carbonate minerals in Well N1, Well Y1 and Well W1.

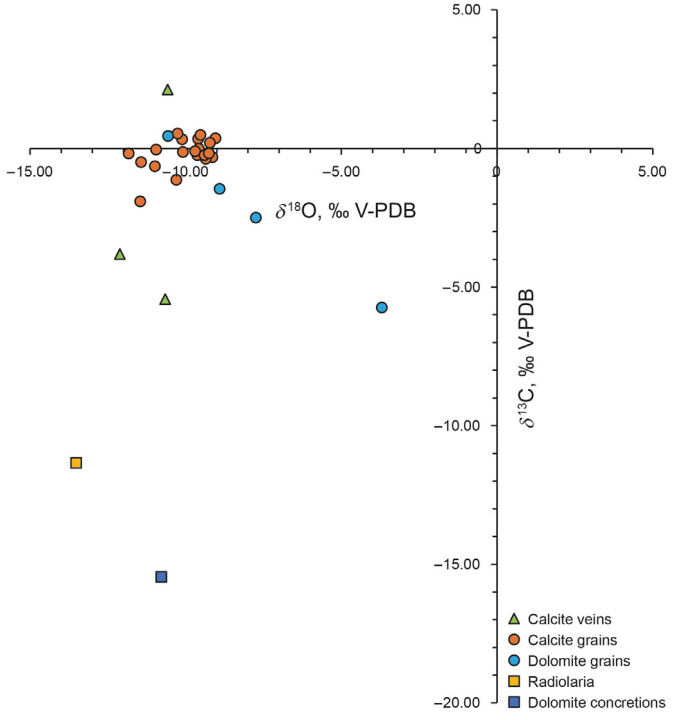

Fig. 11. Inorganic carbon and oxygen isotope ratios of carbonate minerals.

(Given and Wilkinson, 1985), but instead aggregating that the nano-scale calcite grains with smooth surface were formed (Fig. 4d).

The morphology of carbonate minerals formed by the microbial activity is complex and variable, and is related to the types of microorganism and the environmental conditions. Common morphologies can include dumbbell-shaped, spherical and hemispherical (Wright and Wacey, 2005; Lian et al., 2006). The calcite formed via microbial growth has different characteristics from calcite grains of inorganic sources. Calcite associated with microorganisms tends to have enriched or depleted $\delta^{13}C$ values. Since the $\delta^{13}C$ values of calcite grains in these samples range from −1.91‰ to 0.54‰, a microbial origin for the calcite grains in this study can be excluded.

A relative depletion of LREE over HREE, prominent positive Y and La anomalies, a positive Gd anomaly and a well-developed negative Ce anomaly indicate that the calcite grains were formed in the oxidizing environment of seawater rather than the reducing environment in pore water (Allwood et al., 2010). The calcite grains in the Longmaxi Shale appear to have originated from marine carbonates formed by a precipitation from oxidizing seawater and then transported to the deep-water shelf environments. The edges of calcite grains show the effects of differential compaction, indicating that the calcite belong to primary sediments.

Dereuil and Birgenheier (2019) demonstrated that carbonate minerals in the Mancos shale (USA) have been transported and deposited by contour current and storm waves up to a distance of 250 km. Carbonate minerals in the Barnett shale in Texas were transported to the deep basin from the continental shelf or upper oxygenated slope by turbidity currents and debris flows (Loucks and Ruppel, 2007). The calcite content of Well Y1, which is located in subsidence center of the southern Sichuan Basin (Fig. 1), is generally low, while the calcite contents of Well N1 near the Qianzhong Uplift (old land) and Well W1 near the Chuanzhong submarine high are relatively high. These high carbonate mineral

Table 2
Bulk rock carbon and oxygen isotopes.

Sample ID	Calcite, %	Dolomite, %	Carbonate mineral type	$\delta^{13}C$, ‰ V-PDB	$\delta^{18}O$, ‰ V-PDB
W1-1	21.20	8.10	Calcite grain	−1.13	−10.30
W1-4	34.20	4.00		−0.49	−11.43
W1-5	34.20	4.20		−1.91	−11.47
W1-6	22.10	6.00		0.33	−10.12
W1-7	23.50	8.10		0.54	−10.26
W1-8	17.90	7.20		−0.12	−10.09
W1-9	30.10	8.10		−0.64	−11.00
N1-2	31.10	8.39		0.21	−9.23
N1-3	22.88	3.80		0.35	−9.60
N1-4	17.00	5.54		0.37	−9.05
N1-5	13.52	2.85		−0.01	−9.58
N1-6	18.80	2.62		0.49	−9.53
N1-7	10.22	3.08		−0.31	−9.15
N1-8	7.12	1.41		−0.24	−9.63
N1-9	10.10	1.92		−0.10	−9.70
N1-10	12.73	3.94		−0.37	−9.36
N1-11	11.92	2.44		−0.18	−11.83
N1-13	14.06	4.10		−0.24	−9.40
N1-14	9.86	0.80		−0.04	−10.96
N1-16	27.05	7.89		−0.17	−9.26
Y1-2	7.00	18.30	Dolomite grain	−5.74	−10.57
W1-3	12.80	31.70		−1.45	−7.75
N1-12	12.19	32.56		−2.49	−8.91
N1-15	9.82	33.20		0.45	−3.71
Y1-3	70.80	1.30	Calcite in radiolaria	−11.34	−13.52
Y1-1	0.90	52.20	Dolomite nodule	−15.46	−10.79
W1-2			Calcite vein	−5.44	−12.12
N1-1				−3.81	−10.58

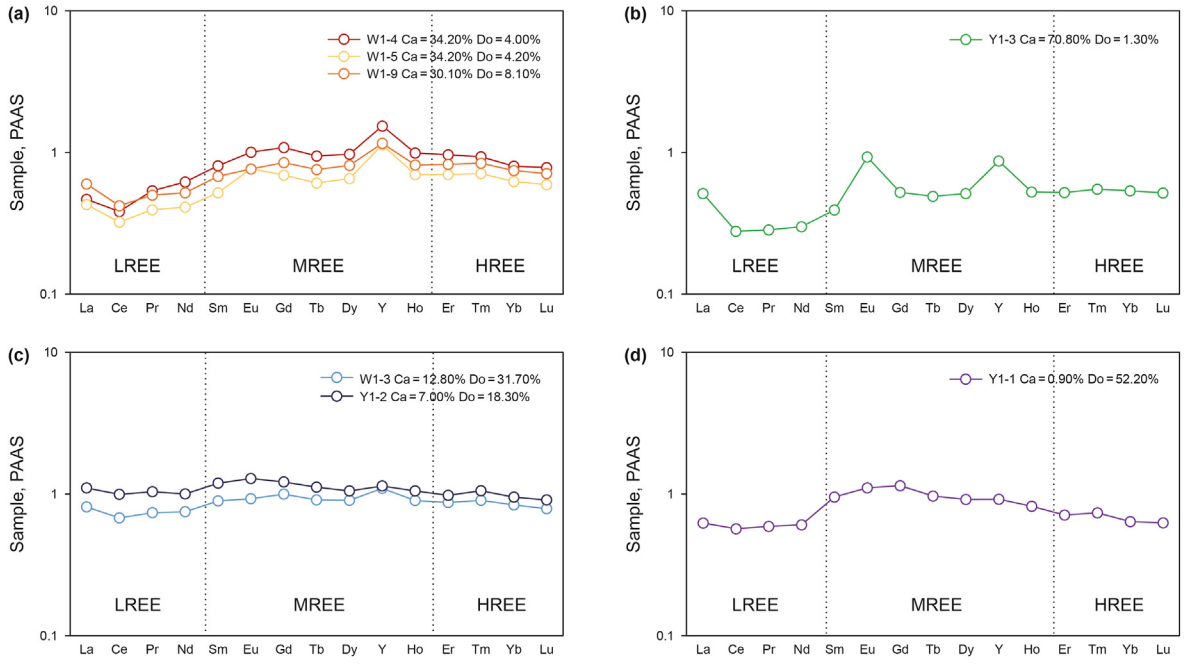

Fig. 12. Rare earth elements and yttrium pattern: (a) PAAS normalized REE + Y patterns for calcite grains; (b) PAAS normalized REE + Y patterns for calcite in radiolarian; (b) PAAS normalized REE + Y patterns for dolomite grains; (d) PAAS normalized REE + Y patterns for dolomite concretions.

contents in these wells suggest a derivation from a carbonate dominated source area and a comparatively short transport path (Schieber and Shao, 2021).

5.1.2. Dolomite grains

The differentially compacted edge of dolomite grain indicates that the ankerite rims are formed in the shallow burial stage of early diagenesis, and the rhombic dolomite grains are a result of

Table 3
The results of rare earth elements and yttrium (μg/g).

Sample ID	W1-4	W1-5	W1-9	Y1-2	W1-3	Y1-1	Y1-3
Calcite, %	34.20	34.20	30.10	7.00	12.80	0.90	70.80
Dolomite, %	4.00	4.20	8.10	18.30	31.70	52.20	1.30
Carbonate mineral type	Calcite grain			Dolomite grain		Dolomite nodule	Calcite in radiolaria
La_N	0.46	0.42	0.60	1.10	0.81	0.62	0.51
Ce_N	0.38	0.32	0.42	0.99	0.67	0.56	0.27
Pr_N	0.53	0.39	0.50	1.03	0.73	0.59	0.28
Nd_N	0.62	0.41	0.52	1.00	0.75	0.60	0.29
Sm_N	0.80	0.52	0.67	1.19	0.89	0.95	0.39
Eu_N	1.00	0.76	0.76	1.28	0.92	1.10	0.93
Gd_N	1.08	0.69	0.84	1.21	0.99	1.14	0.52
Tb_N	0.94	0.61	0.75	1.11	0.90	0.96	0.49
Dy_N	0.97	0.65	0.81	1.05	0.90	0.91	0.51
Y_N	1.53	1.13	1.16	1.13	1.09	0.91	0.87
Ho_N	0.99	0.69	0.81	1.05	0.89	0.82	0.52
Er_N	0.96	0.70	0.82	0.97	0.87	0.71	0.52
Tm_N	0.93	0.71	0.84	1.05	0.90	0.73	0.55
Yb_N	0.80	0.62	0.74	0.95	0.83	0.63	0.53
Lu_N	0.78	0.59	0.71	0.90	0.78	0.62	0.51
La/La*	1.25	1.19	1.30	0.99	1.15	1.12	2.04
Ce/Ce*	0.76	0.78	0.76	0.93	0.88	0.94	0.70
Eu/Eu*	1.07	1.27	1.00	1.07	0.98	1.05	2.02
Gd/Gd*	1.18	1.23	1.20	1.02	1.09	1.13	1.12
Y/Ho	1.55	1.62	1.42	1.08	1.22	1.12	1.65

$La/La^* = La_N/(3Pr_N-2Nd_N)$, $Ce/Ce^* = 2Ce_N/(La_N + Pr_N)$, $Eu/Eu^* = 2Eu_N/(Sm_N + Gd_N)$, $Gd/Gd^* = Gd_N/(2Tb_N-Dy_N)$.

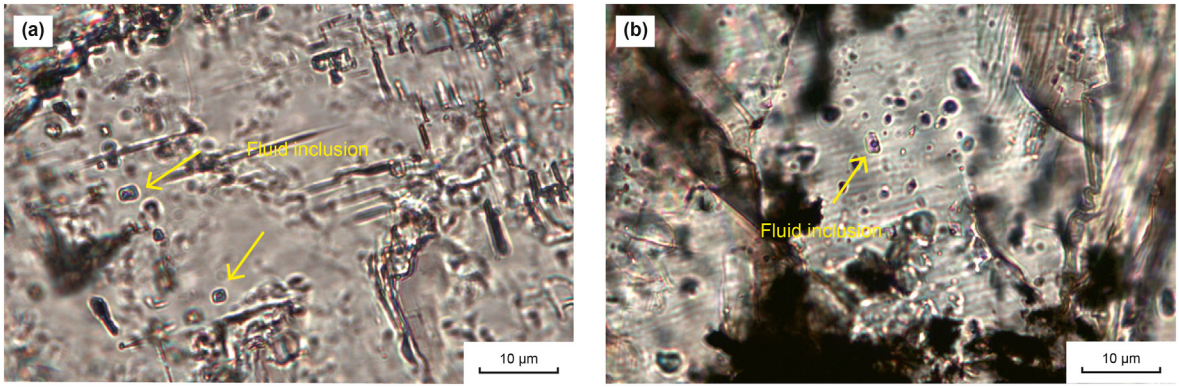

Fig. 13. Fluid inclusions in calcite veins.

Table 4
Homogenization temperatures of the inclusions in the calcite veins.

	Point 1	Point 2	Point 3	Point 4	Point 5
Temperature, °C	153.10	146.70	181.10	182.90	162.50
	Point 6	Point 7	Point 8	Point 9	
Temperature, °C	164.30	169.00	174.60	171.10	

slow growth rates (Cheng et al., 2021). In sulfate-driven anaerobic oxidation of methane (SD-AOM) below microbial sulfate reduction (MSR), the inhibition of dolomite precipitation is weakened due to the decrease in the SO_4^{2-} concentration (Berner et al., 1970; Baker and Kastner, 1981; Compton, 1988). At the same time, the increase of alkalinity of the pore fluids due to MSR also promotes the precipitation of dolomite (Berner et al., 1970). Curtis (1980) and Zhou (2022) proposed that ankerite precipitates during the AOM.

The REE + Y patterns of dolomite grains have no obvious positive and negative anomalies and are a result of the influence of the ankerite rims. Due to the relatively high concentrations of REE in terrestrial detritus and the low concentrations of REE in the shale, even a small contribution of REE (1~2%) from terrigenous clastic inputs will greatly reduce the La anomaly, the Ce anomaly and the uptake consumption degree of LREE during ankerite precipitation. Consequently, the distribution patterns of the REE will be relatively flat (Nothdurft et al., 2004). The conversion of smectite to illite can release a large amount of metal cations such as Ca^{2+}, Mg^{2+} and Fe^{3+} (Ma et al., 2019). The CO_2 produced by SD-AOM also can provide carbon for ankerite rim precipitation.

Similar to the calcite contents, the dolomite contents in the areas of maximum basin subsidence center are low, while they are high at the edge of the basin where the subsidence is limited. This may reflect the clastic source of dolomite cores. Dolomite grains in the Barnett Shale have a variety of different shapes ranging from highly euhedral to anhedral, and are known to be of clastic origin (Loucks and Ruppel, 2007; Milliken et al., 2012). Dolomitic black shale in the Portwood Member of the New Albany Formation in the western Appalachian Basin contains a high content of silt-scale

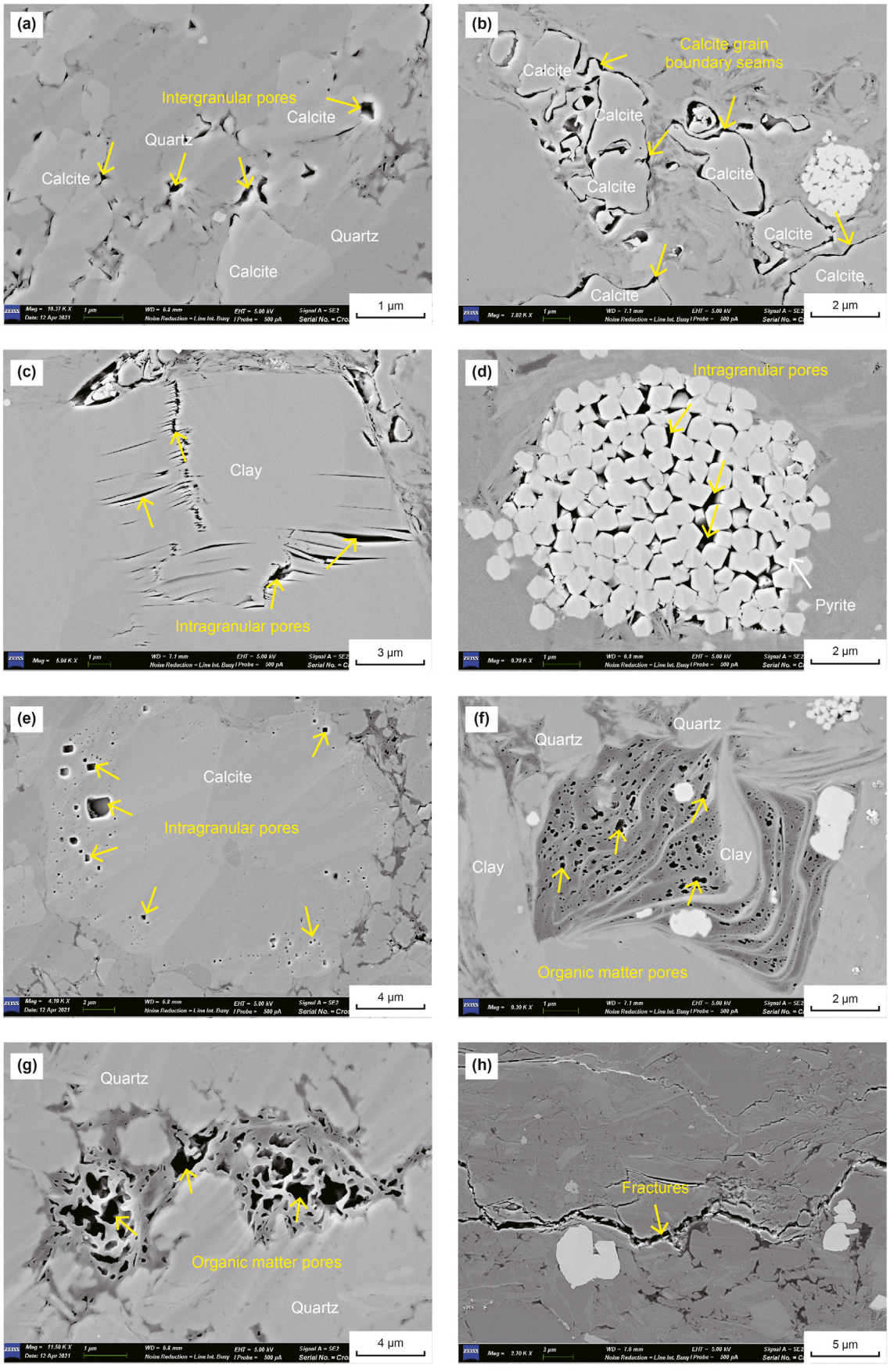
(a)
Intergranular pores
Calcite
Quartz
Calcite
Quartz
Calcite
1 μm
(b)
Calcite grain boundary seams
Calcite
Calcite
Calcite
Calcite
Calcite
Calcite
Calcite
2 μm
(c)
Clay
Intragranular pores
3 μm
(d)
Intragranular pores
Pyrite
2 μm
(e)
Calcite
Intragranular pores
4 μm
(f)
Quartz
Quartz
Clay
Clay
Organic matter pores
2 μm
(g)
Quartz
Organic matter pores
Quartz
4 μm
(h)
Fractures
5 μm

Table 5
Results from MIP and low-temperature nitrogen physisorption tests.

Sample ID	Calcite, %	Dolomite, %	TOC, %	Carbonate mineral type	$\Phi_{porosity}$, %	V_{DFT}, cm^3/g
Y1-4	0.3	0.6	0.88	Calcite and dolomite grain	0.67	0.0096
Y1-5	2.5	6.7	1.69		1.39	0.0123
Y1-6	4.3	3.4	3.40		1.15	0.0133
Y1-7	8.1	1.6	5.51		0.53	0.0054
Y1-8	13.0	8.0	3.40		1.65	0.0142
Y1-9	10.9	7.5	3.97		2.19	0.0173
W1-3	12.8	31.7	4.27		3.16	0.0182
W1-4	34.2	4.0	3.92		2.45	0.0133
W1-6	22.1	6.0	2.82		3.31	0.0162
W1-9	30.1	8.1	2.35		0.92	0.0169
W1-10	3.1	3.3	1.56		2.91	0.0158
W1-11	1.3	1.7	2.35		2.51	0.0169
W1-12	5.2	4.0	1.83		2.11	0.0070
W1-13	8.9	6.7	1.95		1.85	0.0200
W1-14	14.5	8.7	5.03		4.22	0.0226
W1-15	10.2	17.2	2.95		2.70	0.0180
Y1-3	70.8	1.3	0.68	Calcite in radiolaria		0.0015
Y1-10	4.0	5.0	5.51			0.0327
W1-16	4.3	2.5	5.26			0.0165

dolomite grains with irregular shaped and cloudy cores surrounded by clear overgrowths, which appear largely to be of detrital origin. (Schieber and Shao, 2021).

5.1.3. Calcite cements

The calcite cement is mainly distributed in silt-rich laminae (Dowey and Taylor, 2020). The sediment accumulation rate is an important factor affecting cementation in shale (Zou et al., 2015). The Wufeng and Longmaxi Shale were deposited in a semi-deep and deep shelf environment with a slow accumulation of sediments, so calcite cementation is usually highly localized near the sediment/water interface (Milliken and Day-Stirrat, 2013).

As a result of the exothermic characteristic of carbonate dissolution in water, the solubility of carbonate minerals increases gradually with depth in seawater (Denny et al., 2020). Dissolution of carbonate minerals provides a material source for calcite cement. In addition, transformation of clay minerals can also be a source of Ca^{2+} (Ma et al., 2019). Marine shale can be rich in bioclasts and the dissolution of detrital carbonate and bioclasts during early diagenesis can provide calcium and carbon for the dolomite precipitation (Dutton, 2008; Morad et al., 2010; Yang et al., 2018).

5.1.4. Dolomite concretions

The primary fine-grained clay matrix between the dolomite crystals suggests dolomite concretions formed in early, uncompacted argillaceous sediments when they were still relatively soft and unconsolidated (Meister et al., 2007). The euhedral pyrite in dolomite concretions indicates that the dolomite precipitated after the formation of the euhedral pyrite (Dowey and Taylor, 2020). The carbon isotopic signature of dolomite in deep-sea sediments is closely related to that of sulfate reducing bacteria (Friedman and Murata, 1979). Sample of dolomite concretions has a $\delta^{13}C$ of −15.46‰ which is consistent with the carbonate formed in sulfate reduction zone. The MSR in marine sediments causes the precipitation of pyrite and can increase alkalinity in pore fluid, it may promote carbonate precipitation (Berner et al., 1970). The dolomite precipitation in organic-rich marine sediments is inhibited by high sulfate content in pore water and dolomite may form at the bottom of sulfate reduction zone (Compton, 1988). In the SD-AOM, the alkalinity in fluids increase when undergoing MSR and the decrease in the SO_4^{2-} concentrations cause precipitation of dolomite concretions (Berner et al., 1970; Baker and Kastner, 1981; Compton, 1988).

REE + Y patterns of dolomite concretions are characterized by MREE enrichment and LREE and HREE depletion, which is similar to what is observed in the dolomite and thin limestone in the Doushantuo Formation in the Jiulongwan section of China (Huang et al., 2009). This pattern is often interpreted as a record of the REE distribution in seawater that has modified by iron and manganese oxides in an anoxic environment below the water/sediment interface (Haley et al., 2004). In shale diagenesis, pyrite formed in the MSR can alter the concentrations and distributions of rare earth elements in pore water, including enrichment of MREE in pore water (Nédélec et al., 2007).

5.1.5. Calcite in radiolarian

The occurrences of abundant anhedral pyrites and the $\delta^{13}C$-deficit calcite (−11.34‰) in radiolarian indicate the formation of calcite may be related to the occurrence of MSR, which lead to pyrite formation (Berner et al., 1970; Cai et al., 2021). The pyrite formation in MSR greatly increases the alkalinity of pore fluid and can enhance the precipitation of calcite with depleted $\delta^{13}C$ values since the CO_3^{2-} originates in part from organic matter via MSR (Berner et al., 1970; Cai et al., 2021).

In the low-temperature stage of early diagenesis, microcrystalline quartz in radiolarian-rich mudstones formed from the dissolution and reprecipitation of siliceous bioskeletons (Milliken, 2014; Schieber et al., 2000; Zhao and Jin, 2021). At the dissolution of siliceous bioskeletons, calcite precipitationin in radiolarian. The sample has a significant positive Eu anomaly which may be caused by dissolution of Ca-plagioclase in which the enrichment of Eu, especially Eu^{2+}, is more significant than other REEs (Lee et al., 2003;

Fig. 14. Microscopic characteristics of pore types and fractures: (a) SEM image of intergranular pores between microcrystalline quartz and calcite grains (Sample Y1-7); (b) SEM image of calcite grain boundary seams (Sample Y1-8); (c) SEM image of intragranular pores within clay mineral (Sample Y1-8); (d) SEM image of intragranular pores within framboidal pyrite (Sample Y1-4); (e) SEM image of intragranular pores in calcite grains (Sample Y1-13); (f) SEM image of organic pores (Sample Y1-13); (g) SEM image of organic pores (Sample Y1-8); (h) SEM image of fractures (Sample Y1-14).

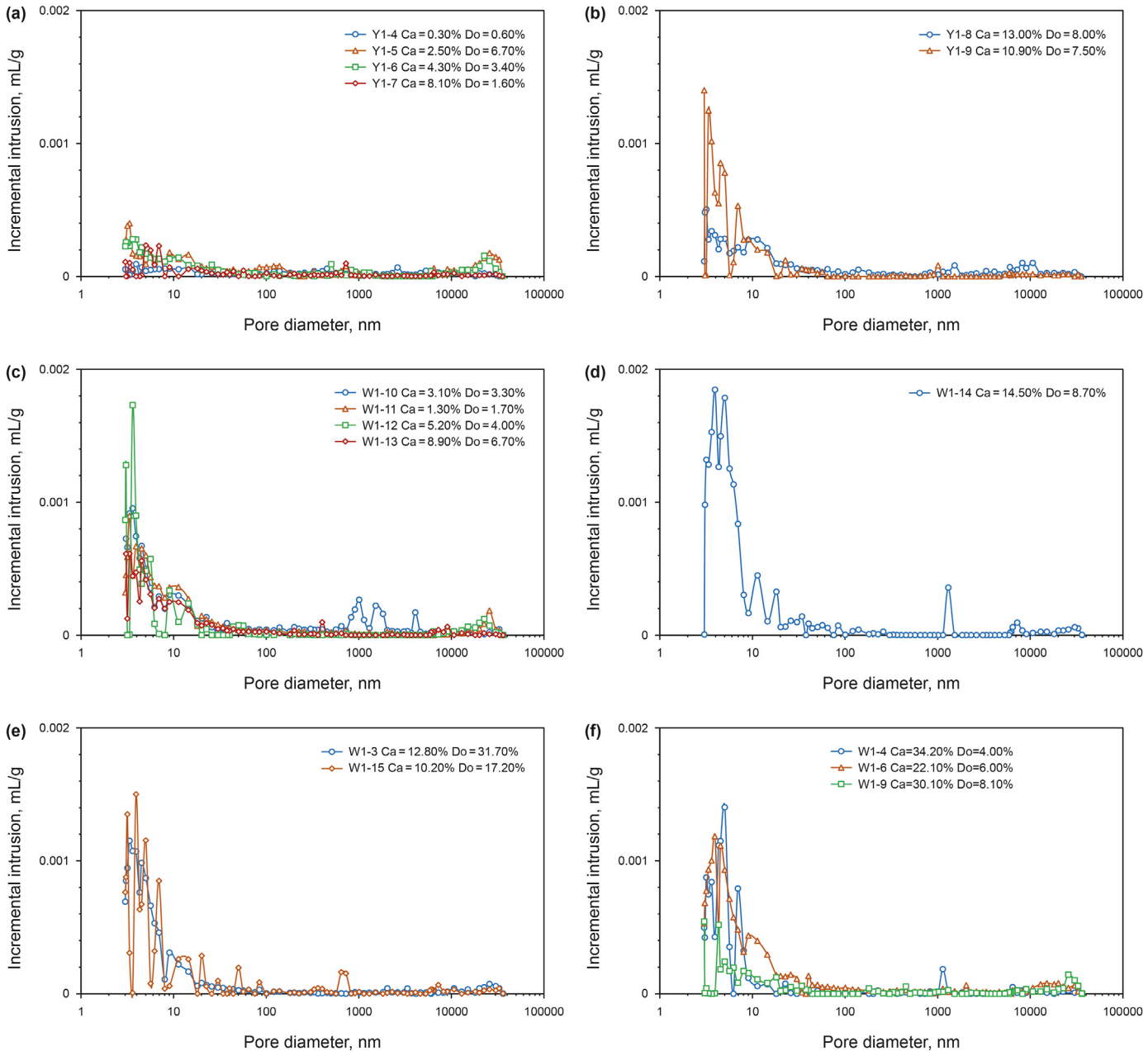

Fig. 15. Relationship between pore diameter and incremental mercury intrusion (Ca: calcite content; Do: dolomite content).

Barker et al., 2006; Cai et al., 2008; Wang et al., 2017; Gao et al.,2019). Eu^{2+} can replace Ca^{2+} during calcite precipitation, resulting in a positive Eu anomaly in the calcite in radiolarian.

5.1.6. Calcite veins

Fibrous calcite veins parallel to bedding planes are common in organic-rich and carbonate-rich black shales (Rodrigues et al., 2009; Tribovillard et al., 2018). Temperature measurements from gas-liquid two-phase brine inclusions in calcite veins show veins are precipitated in the deep burial stage. Thermal decarboxylation of organic matter can produce carbon dioxide with $\delta^{13}C$ values ranging from −8‰ to −23‰ (V-PDB) (Sensuła et al., 2006). Temperature measurement results of inclusions and the $\delta^{13}C$ values (−5.44‰, −3.81‰) indicate that there are other sources of the CO_3^{2-} required for calcite vein precipitation in addition to CO_2 generated by thermal decarboxylation. Combined with the dissolution phenomenon at the edges of calcite grains, dissolution of calcite in surrounding rock may also be involved in the formation of veins (Heydari and Wade, 2002; Zhang et al., 2016; Gao et al., 2019; Luan et al., 2019).The most commonly accepted explanation for the mechanism of opening the space in which the fibrous calcite vein is emplaced is overpressure caused both by petroleum generation and the dehydration of clay-minerals (illitization of smectite) (Ramsay, 1980; Oliver and Bons, 2001; Wang et al., 2018).

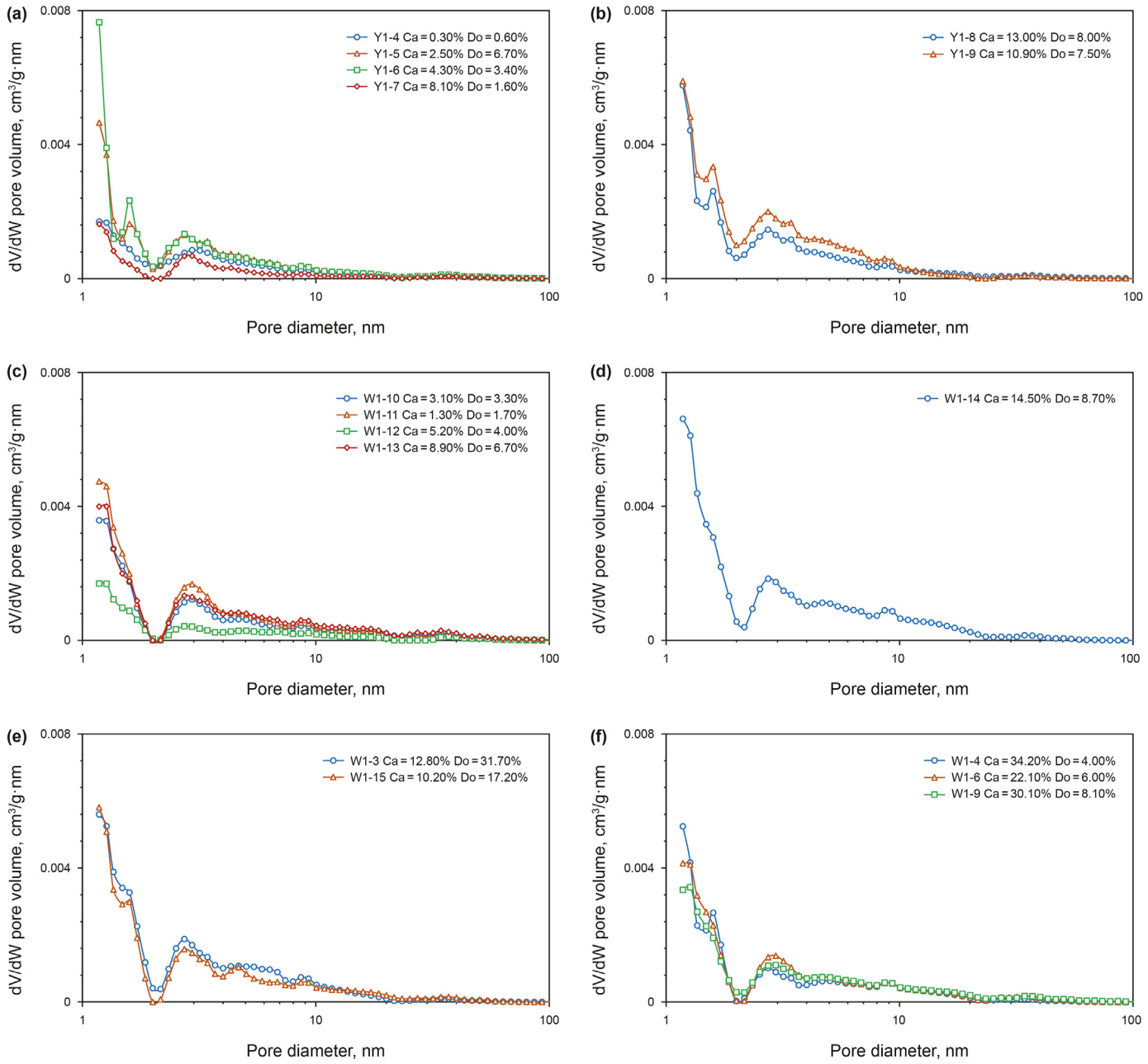

Fig. 16. Pore diameter distribution in samples of calcite and dolomite grains.

Table 6
Influence of calcite and dolomite contents on porosity and pore volume of samples.

	Well Y1		Well W1	
	Average porosity, %	Average pore volume, cm^3/g	Average porosity, %	Average pore volume, cm^3/g
Calcite content < 10% Dolomite content < 10%	0.93	0.0102	2.34	0.0149
10% < Calcite content < 20% Dolomite content < 10%	1.92	0.0158	4.22	0.0226
10% < Calcite content < 20% Dolomite content > 10%			2.93	0.0181
Calcite content > 20% Dolomite content < 10%			2.23	0.0155

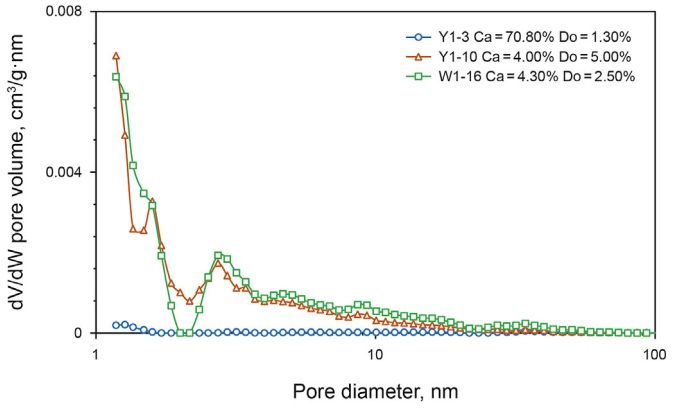

Fig. 17. Pore diameter distribution in samples of radiolarian.

5.2. Effects of carbonate minerals on shale reservoirs

In samples, we can observe that the space between minerals is almost completely filled with organic matter under SEM and organic pores are often developed in organic matter (Fig. 14e–g, Fig. 18a–b, d, g–h). Samples in this study with low carbonate mineral content have low TOC and few organic pores, mainly mesopores (2–50 nm) (Fig. 18a). For example, sample of Y1-4 have 0.3% calcite and 0.6% dolomite, and a TOC content of 0.88%. Samples with high carbonate mineral content have relatively high TOC content and abundances of organic pores, mainly mesopores (2–50 nm) (Fig. 18b). For example, Sample Y1-8 have 13.0% calcite and 8.0% dolomite, and a TOC of 3.40%. TOC has a good positive correlation with porosity (measured by MIP tests) (Fig. 19). Therefore, we believe that the difference of porosity in shale is mainly caused by organic matter pores. Differences in the distribution of pore size between samples are mainly in the range of 1–20 nm pore diameter in MIP tests (Fig. 16). Previous studies have shown that the primary controlling factor for the development of nanopores is the content of organic matter in shale (Loucks et al., 2009; Tian et al., 2013; Yang et al., 2016).

The samples of radiolarian partly filled with calcite have relative high pore volumes and high TOC contents (Fig. 17, Table 6). Similar to the Chattanooga Shale, Barnett Shale and Mowry Shale, the dissolution and reprecipitation of siliceous bioskeletons formed microcrystalline authigenic quartz (Schieber et al., 2000; Milliken, 2014; Zhao and Jin, 2021) (Fig. 18g). When radiolarian are partially filled with subhedral calcite in siliceous shale, primary storage space is preserved between the calcite and the surrounding microcrystalline quartz (Fig. 18h; Fig. 21).

Based on the organic matter maturity, the diagenesis stage of shale can be divided into early diagenesis stage, middle diagenesis stage and late diagenesis stage. During the early diagenesis stage, argillaceous sediments quickly release a large amount of pore water and porosity of shale decrease rapidly because of increasing overburden pressure (Baldwin and Butler, 1985). The rigid framework formed by calcite and the surrounding microcrystalline quartz plays an important role in preservation of organic matter. In the oil window, kerogen cracks to generate petroleum, pores are formed inside the kerogen, and liquid and gaseous petroleum can migrate into the intergranular pores preserved by carbonate minerals (Löhr et al., 2015) (Fig. 21). Thermal cracking of liquid petroleum during late diagenesis will generate solid organic residues that can then develop organic porosity (Bernard and Horsfield, 2014; Cardott et al., 2015) (Fig. 21).

However, the sample of radiolarian completely filled with calcite in calcareous shale have very low pore volumes and low TOC contents (Fig. 17, Table 6). The inorganic pores in calcite in radiolarian are mainly isolated intragranular pores and are frequently filled with organic matter (Fig. 18e and f). The protective effect of rigid framework is destroyed, which results in the degradation of the reservoir properties.

When calcite contents are < 10%, the total pore volumes of shale samples are low (Fig. 15a, c; Fig. 16a, c; Table 6), and there is no relationship between calcite content and porosity (from MIP tests) (Fig. 20). In this situation, porosity in shales is mainly controlled by other minerals (clay minerals, feldspar and quartz). However, when the calcite contents are in the range of 10%–20%, shale samples have high total pore volumes (Fig. 15b, d–e; Fig. 16b, d–e; Table 6), and there is a positive correlation between calcite content and porosity (Fig. 20). Compared with fine-grained clay-rich sedimentary rocks, clastic-derived calcite grains and calcite cement in silty and siliceous shale formed in the early diagenesis stages are more resistant to compaction and tend to form a relatively rigid framework that is more conducive to preservation of large pores. (Jarvie et al., 2007; Sone and Zoback, 2013). Liquid petroleum can fill the storage space and the cracking of liquid petroleum will generate solid organic residues that can then develop organic porosity. (Fig. 21). However, when the calcite contents are > 20%, the total pore volumes and TOC contents decrease significantly (Fig. 15f; Fig. 16f; Fig. 20; Table 6). The reason may be that the high calcite grain content represents strong input of terrestrial detritus. In addition, at this time, the sea level is relatively low and preservation of organic matter is weak, resulting in a decrease in porosity. The dolomite contents are < 10% in most samples, and there are only two samples with dolomite contents large than 10% (Fig. 20). The influence of dolomite grains on shale reservoirs are not clear.

During the middle diagenesis stage, organic acids produced by petroleum generation can dissolve carbonates along the edges of the minerals, resulting in irregular grain boundary which have widths of 100–300 nm (Fig. 18c). The dissolution remnants of calcite have jagged edges (Fig. 18d) and provide space for petroleum storage (Fig. 21). In the New Albany Shale, Maquoketa shale and Geneseo shale, a partial dissolution along the edges of carbonate grains is common, resulting in carbonate mineral seam with irregular pore shape or rectangular outline (Schieber, 2010). In carbonate-rich shale, dissolution pores in carbonate mineral may enhance natural gas migration.

6. Conclusions

The inorganic carbon and oxygen isotope tests and rare earth elements and yttrium concentrations are effective tools to determining the genesis and diagenetic evolution of carbonate minerals. Carbonate minerals formed in different environments during deposition and diagenesis have distinctive isotope and element

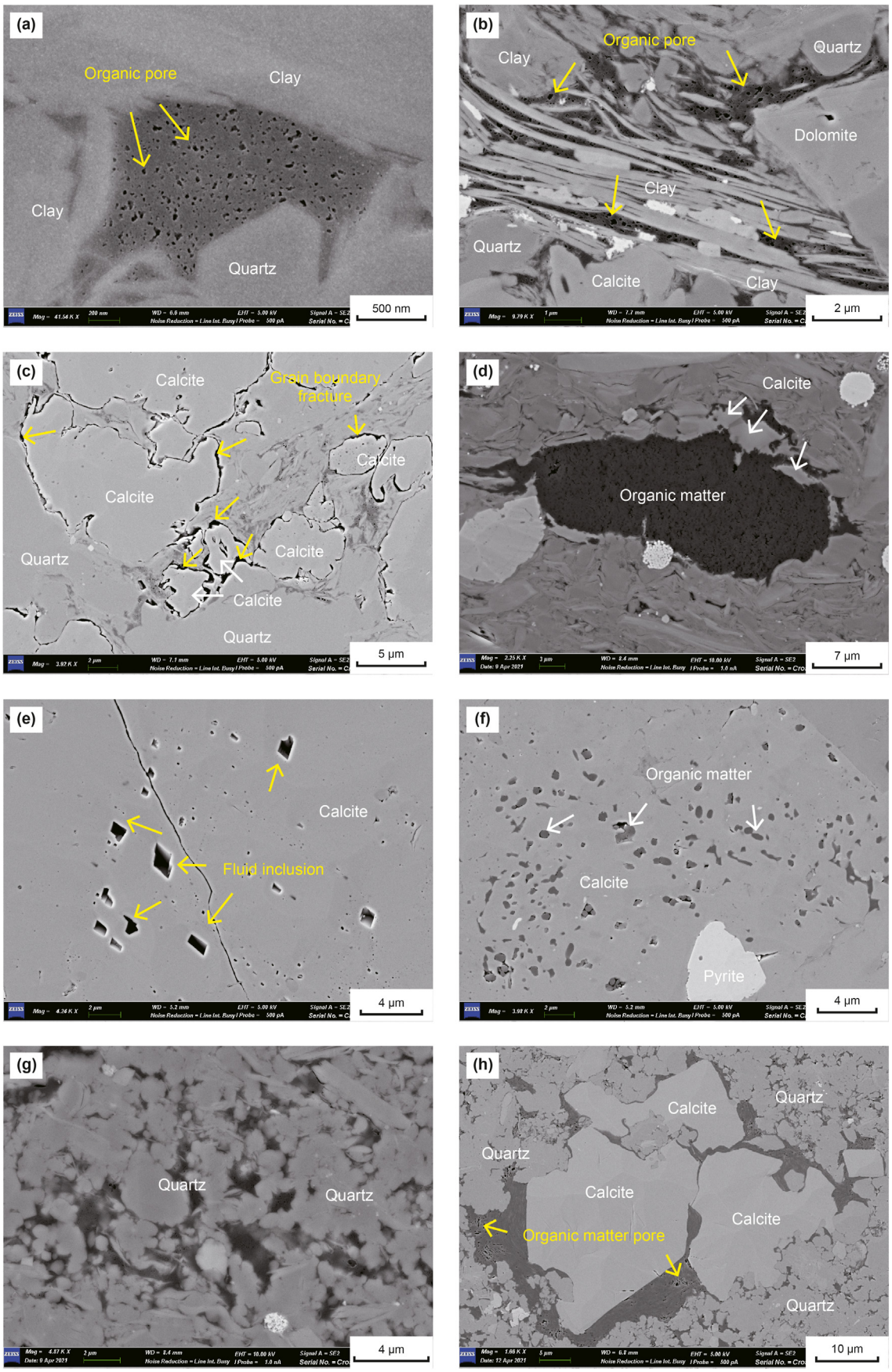
(a)
Organic pore
Clay
Clay
Quartz
500 nm
(b)
Clay
Organic pore
Quartz
Dolomite
Clay
Quartz
Calcite
Clay
2 μm
(c)
Calcite
Grain boundary fracture
Calcite
Calcite
Quartz
Calcite
Calcite
Quartz
5 μm
(d)
Calcite
Organic matter
7 μm
(e)
Calcite
Fluid inclusion
4 μm
(f)
Organic matter
Calcite
Pyrite
4 μm
(g)
Quartz
Quartz
4 μm
(h)
Calcite
Quartz
Quartz
Calcite
Calcite
Organic matter pore
Quartz
10 μm

Fig. 18. Microscopic mineral and pore characteristics: (a) SEM image of nanoscale organic pores in sample with 0.3% calcite and 0.6% dolomite (Sample Y1-4); (b–c) SEM images of organic pores and calcite grain boundary seam in sample with 13.0% calcite and 8.0% dolomite (Sample Y1-8); (d) SEM image of organic matter and serrated edges of residual calcite from dissolution (Sample Y1-15); (e–f) SEM images of intragranular pores of calcite in radiolarian (Sample Y1-3); (g) SEM image of microcrystalline quartz (Sample Y1-10); (h) SEM image of subhedral calcite in radiolarian (Sample Y1-10).

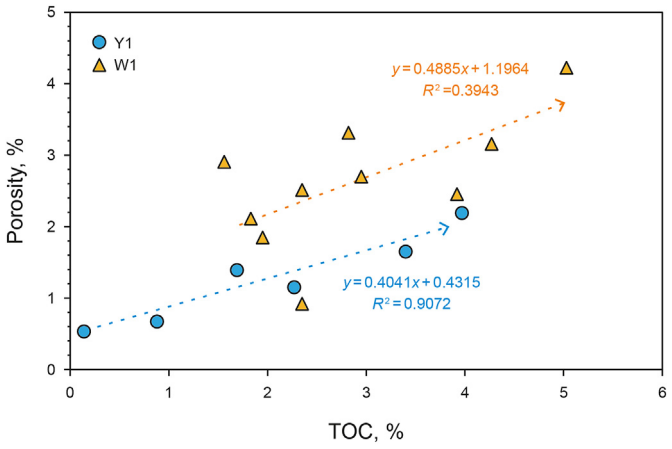

Fig. 19. Relationships between TOC and porosity of carbonate minerals.

characters. The results show that carbonate minerals of clastic source, calcite precipitated in MSR and dolomite formed in SD-AOM all exist in Wufeng and Longmaxi Shale in the Sichuan Basin of southern China. Different types and contents of carbonate minerals lead to differences in the gas storage capacity of shales. The SEM imaging, MIP tests and low-pressure nitrogen physisorption experiments can reflect the pore size distribution of shale. Carbonate minerals perform similarly to silty minerals (quartz and feldspar) in silty shale and siliceous shale. The rigid grain framework formed by calcite grains and calcite cement in silty shale and siliceous shale can enhance reservoir capacity. Organic acids produced by petroleum generation can dissolve carbonate minerals and form grain boundary seam, which are conducive to the formation of a connected pore network. The partly filled calcite in radiolarian in siliceous shale is beneficial to the storage space, while radiolarian completely filled with calcite in calcareous shale will greatly reduce the storage space. The study tries to research the origin and diagenetic evolution of carbonate minerals in shale using conventional testing methods. Innovative experiments are needed in further research.

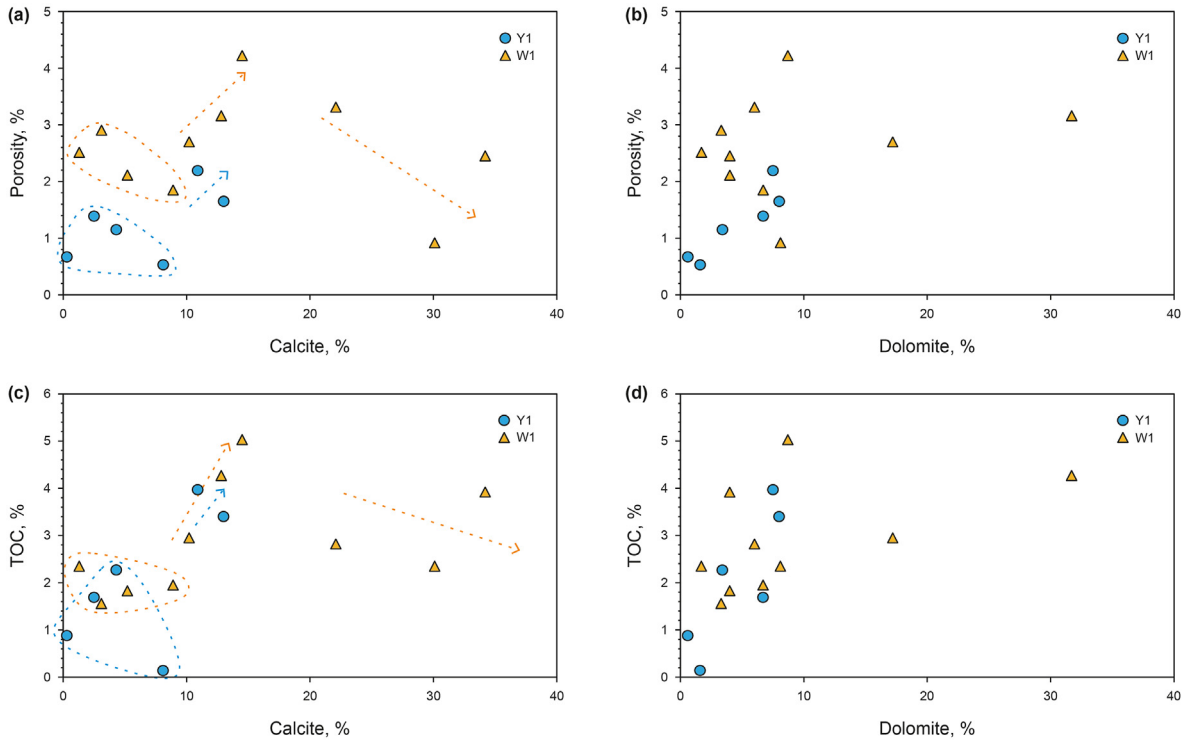

Fig. 20. Relationships between carbonate mineral content, porosity and TOC.

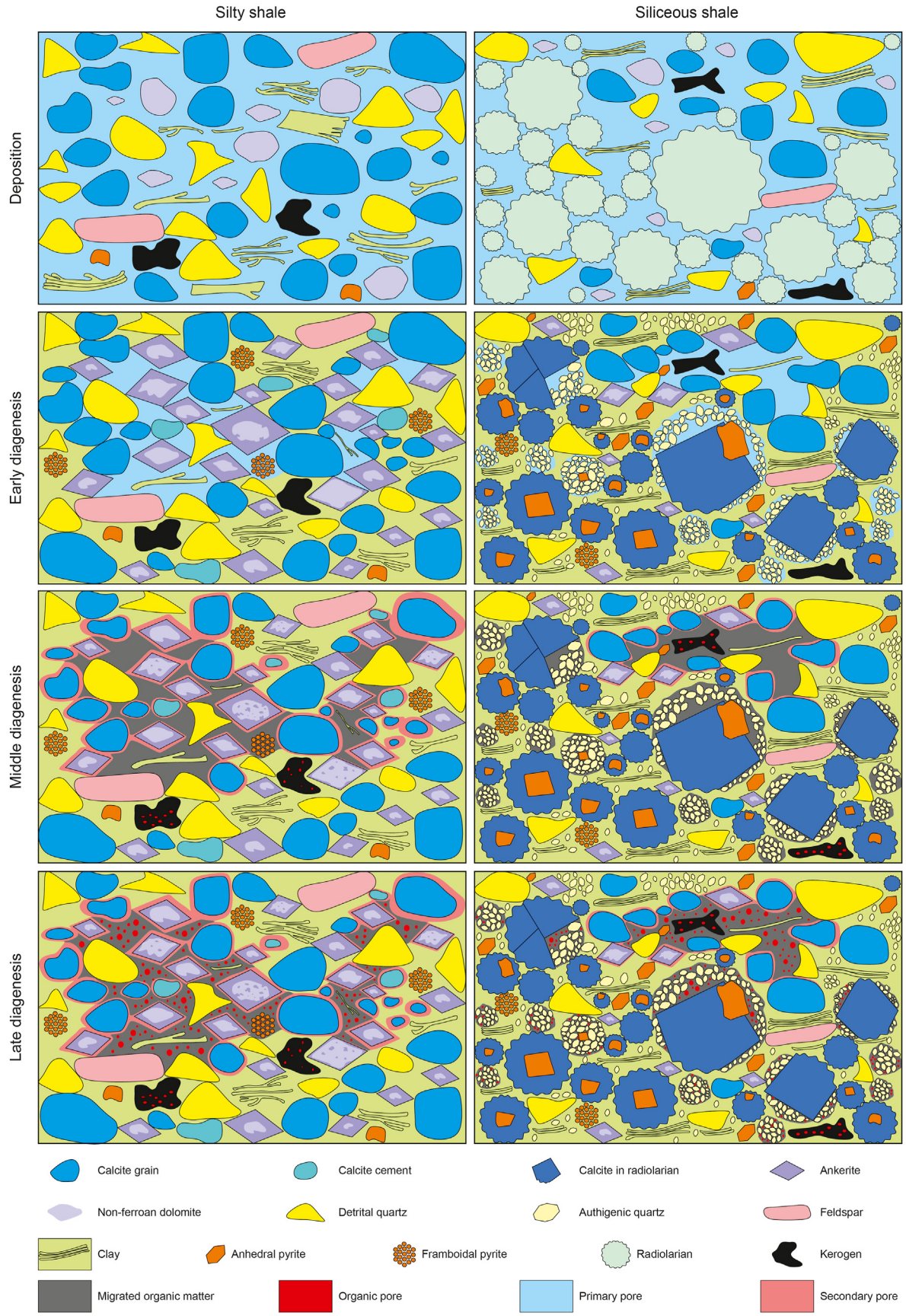

Fig. 21. Schematic diagram of the carbonate minerals influence on physical properties of reservoir.

Declaration of competing interest

The authors declare that they have no known competing financial interests or personal relationships that could have appeared to influence the work reported in this paper.

Acknowledgments

This research was supported by the National Natural Science Foundation of China (Nos. 42172148, 41830431, and 41902127). We would like to thank PetroChina Southwest Oil & Gasfield Company for providing shale core samples. Comments and suggestions of Editors and reviewers are gratefully appreciated.

References

Allwood, A.C., Kamber, B.S., Walter, M.R., Burch, I.W., Kanik, I., 2010. Trace elements record depositional history of an Early Archean stromatolitic carbonate platform. Chem. Geol. 270 (1–4), 148–163. https://doi.org/10.1016/j.chemgeo.2009.11.013.

Aplin, A.C., Macquaker, J.H.S., 2011. Mudstone diversity: origin and implications for source, seal, and reservoir properties in petroleum systems. Am. Assoc. Petrol. Geol. Bull. 95 (12), 2031–2059. https://doi.org/10.1306/03281110162.

Baldwin, B., Butler, C.O., 1985. Compaction curves. Am. Assoc. Petrol. Geol. Bull. 69 (4), 622–626. https://doi.org/10.1306/ad462547-16f7-11d7-8645000102c1865d.

Balthasar, U., Cusack, M., 2015. Aragonite-calcite seas-quantifying the gray area. Geology 43 (2), 99–102. https://doi.org/10.1130/G36293.1.

Baker, P.A., Kastner, M., 1981. Constrains on the formation of sedimentary dolomite. Science 213 (4505), 214–216. https://doi.org/10.1126/science.213.4504.214.

Barker, S.L.L., Cox, S.F., Eggins, S.M., Gagan, M.K., 2006. Microchemical evidence for episodic growth of antitaxial veins during fracture-controlled fluid flow. Earth Planet Sci. Lett. 250 (1–2), 331–344. https://doi.org/10.1016/j.epsl.2006.07.051.

Berner, R.A., Scott, M.R., Thomlinson, C., 1970. Carbonate alkalinity in the pore waters of anoxic marine sediments. Limnol. Oceanogr. 15 (4), 544–549. https://doi.org/10.4319/lo.1970.15.4.0544.

Bernard, S., Horsfield, B., 2014. Reply to comment on "formation of nanoporous pyrobitumen residues during maturation of the Barnett Shale (Fort Worth Basin)". Int. J. Coal Geol. 127, 114–115. https://doi.org/10.1016/j.coal.2014.01.005.

Cai, S.Y., Xiao, Q.L., Zhu, W.P., Zhu, H.Q., Chen, J., Chen, Q., Jiang, X.C., 2020. Shale reservoir characteristics and main controlling factors of Longmaxi Formation, Southern Sichuan Basin. Acta Sedimentol. Sin. 39 (5), 1100–1110. https://doi.org/10.14027/j.issn.1000-0550.2020.060 (in Chinese with English abstract).

Cai, C.F., Li, K.K., Li, H.T., Zhang, B.S., 2008. Evidence for cross formational hot brine flow from integrated $^{87}Sr/^{86}Sr$, REE and fluid inclusions of the Ordovician veins in Central Tarim, China. Appl. Geochem. 23 (8), 2226–2235. https://doi.org/10.1016/j.apgeochem.2008.03.009.

Cai, C.F., Li, K.K., Liu, D.W., John, C.M., Wang, D.W., Fu, B., Fakhraee, M., He, H., Feng, L.J., Jiang, L., 2021. Anaerobic oxidation of methane by Mn oxides in sulfate-poor environments. Geology 49 (7), 761–766. https://doi.org/10.1130/G48553.1.

Cardott, B.J., Landis, C.R., Curtis, M.E., 2015. Post-oil solid bitumen network in the Woodford Shale, USA — a potential primary migration pathway. Int. J. Coal Geol. 139 (1), 106–113. https://doi.org/10.1016/j.coal.2014.08.012.

Castanier, S., Levrel, G.L.M., Perthuisot, J.P., 1999. Ca-carbonates precipitation and-limestone genesis-the microbiogeologist point of view. Sediment. Geol. 126 (1–4), 9–23. https://doi.org/10.1016/S0037-0738(99)00028-7.

Chalmers, G.R., Bustin, R.M., Power, T.M., 2012. Characterization of gas shale pore systems by porosimetry, pycnometry, surface area, and field emission scanning electron microscope/transmission electron microscope image analyses: examples from the Barnett, Woodford, Haynesville, Marcellus, and Doig units. Am. Assoc. Petrol. Geol. Bull. 96 (6), 1099–1119. https://doi.org/10.1306/10171111052.

Chen, L., Jiang, Z.X., Liu, Q.X., Jiang, S., Liu, K.Y., Tan, J.Q., Gao, F.L., 2019. Mechanism of shale gas occurrence: insights from comparative study on pore structures of marine and lacustrine shales. Mar. Petrol. Geol. 104, 200–216. https://doi.org/10.1016/j.marpetgeo.2019.03.027.

Chen, X., Rong, J.Y., Charles, E.M., David, A.T.H., Fan, J., Zhan, R., Zhang, Y., Li, R., 2000. Late Ordovician to earliest Silurian graptolite and brachiopod biozonation from the Yangtze region, South China, with a global correlation. Geol. Mag. 137 (6), 623–650. https://doi.org/10.1017/s0016756800004702.

Cheng, J.R., Meng, X.Q., Zhang, E.L., Jiang, Q.F., Ni, Z.Y., Ji, J.F., 2021. An early Holocene primary proto-dolomite layer of abiotic origin in Lake Sayram, Central Asia. Geophys. Res. Lett. 48 (23), 1–13. https://doi.org/10.1029/2021GL096309.

Cobbold, P.R., Zanella, A., Rodrigues, N., Løseth, H., 2013. Bedding-parallel fibrous veins (beef and cone-in-cone): worldwide occurrence and possible significance in terms of fluid overpressure, hydrocarbon generation and mineralization. Mar. Petrol. Geol. 43, 1–20. https://doi.org/10.1016/j.marpetgeo.2013.01.010.

Compton, J.S., 1988. Degree of supersaturation and precipitation of organogenic dolomite. Geology 16 (4), 318–321. https://doi.org/10.1130/0091-7613(1988)016<0318:DOSAPO>2.3.CO;2.

Cui, Y.F., Jones, S.J., Saville, C., Stricker, S., Wang, G.W., Tang, L.X., Fan, X.Q., Chen, J., 2017. The role played by carbonate cementation in controlling reservoir quality of the Triassic Skagerrak Formation, Norway. Mar. Petrol. Geol. 85 (1), 316–331. https://doi.org/10.1016/j.marpetgeo.2017.05.020.

Curtis, C.D., 1980. Diagenetic alteration in black shales. J. Geol. Soc. 137 (2), 189–194. https://doi.org/10.1144/gsjgs.137.2.0189.

Denny, A.C., Orland, I.J., Valley, J.W., 2020. Regionally correlated oxygen and carbon isotope Zonation in diagenetic carbonates of the Bakken formation. Chem. Geol. 531, 119327. https://doi.org/10.1016/j.chemgeo.2019.119327.

Derry, L.A., Kaufman, A.J., Jacobsen, S.B., 1992. Sedimentary cycling and environmental change in the Late Proterozoic: evidence from stable and radiogenic isotopes. Geochem. Cosmochim. Acta 56 (3), 1317–1329. https://doi.org/10.1016/0016-7037(92)90064-.

Dereuil, A.A., Birgenheier, L.P., 2019. Sediment dispersal and organic carbon preservation in a dynamic mudstone-dominated system, Juana Lopez Member, Mancos Shale. Sediment 66 (3), 1002–1041. https://doi.org/10.1111/sed.12532.

Dowey, P.J., Taylor, K.G., 2020. Diagenetic mineral development within the upper Jurassic Haynesville-Bossier Shale, USA. Sediment 67 (1), 47–77. https://doi.org/10.1111/sed.12624.

Dutton, S.P., 2008. Calcite cement in Permian deep-water sandstones, Delaware Basin, west Texas: origin, distribution, and effect on reservoir properties. Am. Assoc. Petrol. Geol. Bull. 92 (6), 765–787. https://doi.org/10.1306/01280807107.

Dupraz, C., Reid, R.P., Braissant, O., Decho, A., Norman, R.S., Visscher, P.T., 2009. Processes of carbonate precipitation in modern microbial mats. Earth Sci. Rev. 96 (3), 141–162. https://doi.org/10.1016/j.earscirev.2008.10.005.

Friedman, I., Murata, K.J., 1979. Origin of dolomite in Miocene Monterey shale and related formations in the temblor range, California. Geochem. Cosmochim. Acta 43 (8), 1357–1365. https://doi.org/10.1016/0016-7037(79)90126-1.

Furmann, A., Mastalerz, M., Bish, D.L., Schimmelmann, A., 2016. Porosity and pore size distribution in mudrocks from the Belle Fourche and Second white Specks formations in Alberta, Canada. Assoc. Petrol. Geol. Bull. 100 (8), 1265–1288. https://doi.org/10.1306/02191615118.

Gallagher, K.L., Kading, T.J., Braissant, O., Dupraz, C., Visscher, P.T., 2012. Inside the alkalinity engine: the role of electron donors in the organomineralization potential of sulfate-reducing bacteria. Geobiology 10 (6), 518–530. https://doi.org/10.1111/j.1472-4669.2012.00342.x.

Gao, J., He, S., Zhao, J.X., He, Z., Wu, C., Feng, Y., Nguyen, A.D., Zhou, J., Yi, Z., 2019. Sm-Nd isochron dating and geochemical (rare earth elements, $^{87}Sr/^{86}Sr$, $\delta^{18}O$, $\delta^{13}C$) characterization of calcite veins in the Jiaoshiba shale gas field, China: implications for the mechanisms of vein formation in shale gas systems. Geol. Soc. Am. Bull. 132 (7–8), 1722–1740. https://doi.org/10.1130/B32015.1.

Given, R.K., Wilkinson, B.H., 1985. Kinetic control of morphology, composition, and Mineralogy of abiotic sedimentary carbonates. J. Sediment. Res. 55 (6), 919–926. https://doi.org/10.1306/212f862a-2b24-11d7-8648000102c1865d.

Guo, T.L., Zhang, H.R., 2014. Formation and enrichment mode of Jiaoshiba shale gas field, Sichuan Basin. Petrol. Explor. Dev. 41 (1), 28–36. https://doi.org/10.1016/S1876-3804(14)60003-3 (in Chinese with English abstract).

Haley, B.A., Klinkhammer, G.P., McManus, J., 2004. Rare earth elements in pore waters of marine sediments. Geochim. Cosmochim. Acta 68 (6), 1265–1279. https://doi.org/10.1016/j.gca.2003.09.012.

Heydari, E., Wade, W.J., 2002. Massive recrystallization of low-Mg calcite at high temperatures in hydrocarbon source rocks: implications for organic acids as factors in diagenesis. Am. Assoc. Petrol. Geol. Bull. 86 (7), 1285–1303. https://doi.org/10.1306/61EEDC7E-173E-11D7-8645000102C1865D.

Hu, Q.H., Ewing, R.P., Rowe, H.D., 2015. Low nanopore connectivity limits gas production in Barnett formation. J. Geophys. Res. Solid Earth 120 (12), 8073–8087. https://doi.org/10.1002/2015JB012103.

Huang, J., Chu, X.L., Chang, H.J., Feng, L., 2009. Trace element and rare earth element of cap carbonate in Ediacaran Doushantuo Formation in Yangtze Gorges. Chin. Sci. Bull. 54 (18), 3295–3302. https://doi.org/10.1007/s11434-009-0305-1 (in Chinese with English abstract).

Jacobsen, S.B., Kaufman, A.J., 1999. The Sr, C and O isotopic evolution of Neoproterozoic seawater. Chem. Geol. 161 (1–3), 37–57. https://doi.org/10.1016/S0009-2541(99)00080-7.

Jarvie, D.M., Hill, R.J., Ruble, T.E., Pollastro, R.M., 2007. Unconventional shale-gas systems: the Mississippian Barnett Shale of north-central Texas as one model for thermogenic shale gas assessment. Am. Assoc. Petrol. Geol. Bull. 91 (4), 475–499. https://doi.org/10.1306/12190606068.

Knauth, L.P., Kennedy, M.J., 2009. The Late Precambrian greening of the earth. Nature 460 (7256), 728–732. https://doi.org/10.1038/nature08213.

Lastoskie, C., Gubbins, K.E., Quirke, N., 1993. Pore size distribution analysis of microporous carbons: a density functional theory approach. J. Phys. Chem. 97 (18), 4786–4796. https://doi.org/10.1021/j100120a035.

Lee, S.G., Lee, D.H., Kim, Y., Chae, B.G., Kim, W.Y., Woo, N.C., 2003. Rare earth elements as indicators of groundwater environment changes in a fractured rock system: evidence from fracture-filling calcite. Appl. Geochem. 18 (1), 135–143. https://doi.org/10.1016/S0883-2927(02)00071-9.

Lian, B., Hu, Q.N., Chen, J., Ji, J.F., Teng, H.H., 2006. Carbonate biomineralization induced by soil bacterium Bacillus megaterium. Geochem. Cosmochim. Acta 70 (22), 5522–5535. https://doi.org/10.1016/j.gca.2006.08.044.

Liu, S.B., Huang, S.J., Shen, Z.M., Lü, Z.X., Song, R.C., 2014. Diagenetic fluid evolution and water-rock interaction model of carbonate cements in sandstone: an example from the reservoir sandstone of the Fourth Member of the Xujiahe Formation of the Xiaoquan-Fenggu area, Sichuan Province, China. Sci. China.

Earth Sci. 57 (5), 1077–1092. https://doi.org/10.1007/s11430-014-4851-2.
Loucks, R.G., Ruppel, S.C., 2007. Mississippian Barnett Shale: lithofacies and depositional setting of a deep-water shale-gas succession in the Fort worth Basin, Texas. Am. Assoc. Petrol. Geol. Bull. 91 (4), 579–601. https://doi.org/10.1306/11020606059.
Loucks, R.G., Reed, R.M., Ruppel, S.C., Jarvie, D.M., 2009. Morphology, genesis, and distribution of nanometer-scale pores in siliceous mudstones of the mississippian barnett shale. J. Sediment. Res. 79 (12), 848–861. https://doi.org/10.2110/jsr.2009.092.
Loucks, R.G., Reed, R.M., Ruppel, S.C., Hammes, U., 2012. Spectrum of pore types and networks in mudrocks and a descriptive classification for matrix-related mudrock pores. Am. Assoc. Petrol. Geol. Bull. 96 (6), 1071–1098. https://doi.org/10.1306/08171111061.
Löhr, S.C., Baruch, E.T., Hall, P.A., Kennedy, M.J., 2015. Is organic pore development in gas shales influenced by the primary porosity and structure of thermally immature organic matter? Org. Geochem. 87, 119–132. https://doi.org/10.1016/j.orggeochem.2015.07.010.
Lowenstein, T.K., 2001. Oscillations in Phanerozoic seawater chemistry: evidence from fluid inclusions. Science 294 (5544), 1086–1088. https://doi.org/10.1126/science.1064280.
Luan, G.Q., Dong, C.M., Azmy, K., Lin, C.Y., Ma, C.F., Ren, L.H., Zhu, Z.Q., 2019. Origin of bedding-parallel fibrous calcite veins in lacustrine black shale: a case study from Dongying Depression, Bohai Bay Basin. Mar. Petrol. Geol. 102 (2019), 873–885. https://doi.org/10.1016/j.marpetgeo.2019.01.010.
Ma, B.B., Cao, Y.C., Eriksson, K.A., Wang, Y., 2019. Carbonate cementation patterns, potential mass transfer, and implications for reservoir heterogeneity in Eocene tight-oil sandstones, Dongying depression, Bohai Bay Basin, China: evidence from petrology, geochemistry, and numerical modeling. Am. Assoc. Petrol. Geol. Bull. 103 (12), 3035–3067. https://doi.org/10.1306/04101917330.
Ma, X.H., Xie, J., 2018. The progress and prospects of shale gas exploration and exploitation in southern Sichuan Basin, NW China. Petrol. Explor. Dev. 45 (1), 161–169. https://doi.org/10.1016/S1876-3804(18)30018-1 (in Chinese with English abstract).
Macquaker, J.H.S., Taylor, K.G., Gawthorpe, R.L., 2007. High-resolution facies analyses of mudstones: implications for paleoenvironmental and sequence stratigraphic interpretations of offshore ancient mud-dominated successions. J. Sediment. Res. 77 (4), 324–339. https://doi.org/10.2110/jsr.2007.029.
Macquaker, J.H.S., Taylor, K.G., Keller, M., Polya, D., 2014. Compositional controls on early diagenetic pathways in fine-grained sedimentary rocks: implications for predicting unconventional reservoir attributes of mudstones. Am. Assoc. Petrol. Geol. Bull. 98 (3), 587–603. https://doi.org/10.1306/08201311176.
Meister, P., McKenzie, J.A., Vasconcelos, C., Bernasconi, S., Frank, M., Gutjahr, M., Schrag, D.P., 2007. Dolomite formation in the dynamic deep biosphere: results from the Peru Margin. Sediment 54 (5), 1007–1032. https://doi.org/10.1111/j.1365-3091.2007.00870.x.
Milliken, K.L., Papazis, P.K., Day-Stirrat, R.J., Dohse, C., Century, 2012. In: Breyer, J.A. (Ed.), Am. Assoc. Petrol. Geol. Mem., 97, pp. 290–321. https://doi.org/10.1306/13321473M97252.
Milliken, K.L., Day-Stirrat, R.J., 2013. Cementation in mudrocks: brief review with examples from cratonic basin mudrocks. In: Chatellier, J., Jarvie, D. (Eds.), Critical Assessment of Shale Resource Plays. Am. Assoc. Petrol. Geol. Mem. 103, pp. 133–150. https://doi.org/10.1306/13401729H5252.
Milliken, K.A., 2014. A compositional classification for grain assemblages in fine-grained sediments and sedimentary rocks — reply. J. Sediment. Res. 84 (12), 1185–1199. https://doi.org/10.2110/jsr.2014.92.
Morad, S., Ramadan, K.A., Ketzer, J.M., De Ros, L.F., 2010. The impact of diagenesis on the heterogeneity of sandstone reservoirs: a review of the role of depositional facies and sequence stratigraphy. Am. Assoc. Petrol. Geol. Bull. 94 (8), 1267–1309. https://doi.org/10.1306/04211009178.
Nie, H.K., Sun, C.X., Liu, G.X., Du, W., He, Z.L., 2019. Dissolution pore types of the Wufeng Formation and the Longmaxi Formation in the Sichuan Basin, south China: implications for shale gas enrichment. Mar. Petrol. Geol. 101, 243–251. https://doi.org/10.1016/j.marpetgeo.2018.11.042.
Nédélec, A., Affaton, P., France-Lanord, C., Charrière, A., Alvaro, J., 2007. Sedimentology and chemostratigraphy of the Bwipe Neoproterozoic cap dolostones (Ghana, Volta Basin): a record of microbial activity in a peritidal environment – Science Direct. Compt. Rendus Geosci. 339 (3–4), 223–239. https://doi.org/10.1016/j.crte.2005.06.002.
Nothdurft, L.D., Webb, G.E., Kamber, B.S., 2004. Rare earth element geochemistry of Late Devonian reefal carbonates, Canning Basin, Western Australia: confirmation of a seawater REE proxy in ancient limestones. Geochem. Cosmochim. Acta 68 (2), 263–283. https://doi.org/10.1016/S0016-7037(03)00422-8.
Oliver, N.H.S., Bons, P.D., 2001. Mechanisms of fluid flow and fluid-rock interaction in fossil metamorphic hydrothermal systems inferred from vein-wallrock patterns, geometry and microstructure. Geofluids 1 (2), 137–162. https://doi.org/10.1046/j.1468-8123.2001.00013.x.
Porter, S.M., 2007. Seawater chemistry and early carbonate biomineralization. Science 316 (5829), 1302. https://doi.org/10.1126/science.1137284.
Porter, S.M., 2010. Calcite and aragonite seas and the de novo acquisition of carbonate skeletons. Geobiology 8 (4), 256–277. https://doi.org/10.1111/j.1472-4669.2010.00246.x.
Qi, L., Gregoire, D.C., 2000. Determination of trace elements in twenty six Chinese geochemistry reference materials by inductively coupled plasma-mass spectrometry. Geostand. Geoanal. Res. 24 (1), 51–63. https://doi.org/10.1111/j.1751-908x.2000.tb00586.x.
Ramsay, J.G., 1980. The crack-seal mechanism of rock deformation. Nature 284, 135–139. https://doi.org/10.1038/284135a0.
Reitner, J., 1993. Modern cryptic microbialite/metazoan facies from Lizard Island (Great Barrier Reef, Australia) Formation and concepts. Facies 29 (1), 3–39. https://doi.org/10.1007/BF02536915.
Reitner, J., Blumenberg, M., Walliser, E.O., Schäfer, N., Duda, J.P., 2015. Methane-derived carbonate conduits from the late Aptian of Salinac (Marne Bleues, Vocontian Basin, France): petrology and biosignatures. Mar. Petrol. Geol. 66, 641–652. https://doi.org/10.1016/j.marpetgeo.2015.05.029.
Rickman, R., Mullen, M., Petre, E., Grieser, B., Kundert, D., 2008. A practical use of shale petrophysics for stimulation design optimization: all shale plays are not clones of the Barnett Shale. In: SPE Annual Technical Conference and Exhibition. https://doi.org/10.2118/115258-MS, 21-24 September, 2008. SPE 115258, Denver, Colorado, USA.
Ries, J.B., 2004. Effect of ambient Mg/Ca ratio on Mg fractionation in calcareous marine invertebrates: a record of the oceanic Mg/Ca ratio over the Phanerozoic. Geology 32 (11), 981–984. https://doi.org/10.1130/G20851.1.
Rodrigues, N., Cobbold, P.R., Loseth, H., Ruffet, G., 2009. Widespread bedding-parallelveins of fibrous calcite ("beef") in a mature source rock (Vaca Muerta Fm, Neuquen Basin, Argentina): evidence for overpressure and horizontal compression. J. Geol. Soc. 166 (4), 695–709. https://doi.org/10.1144/0016-76492008-111.
Schieber, J., Krinsley, D., Riciputi, L., 2000. Diagenetic origin quartz silt in mudstones and implications for silica cycling. Nature 406 (6799), 981–985. https://doi.org/10.1038/35023143.
Schieber, J., 2010. Common themes in the formation and preservation of Intrinsic porosity in shales and mudstones — illustrated with examples across the Phanerozoic. In: SPE Unconventional Gas Conference 23-25 February, 2010. SPE 132370, Pittsburgh, Pennsylvania, USA. https://doi.org/10.2118/132370-MS.
Schieber, J., Shao, X., 2021. Detecting detrital carbonate in shale successions - relevance for evaluation of depositional setting and sequence stratigraphic interpretation – Science Direct. Mar. Petrol. Geol. 130, 105130. https://doi.org/10.1016/j.marpetgeo.2021.105130.
Seaton, N.A., Walton, J., 1989. A new analysis method for the determination of the pore size distribution of porous carbons from nitrogen adsorption measurements. Carbon 27 (6), 853–861. https://doi.org/10.1016/0008-6223(89)90035-3.
Sensuła, B., Böttger, T., Pazdur, A., Piotrowska, N., Wagner, R., 2006. Carbon and oxygen isotope composition of organic matter and carbonates in recent lacustrine sediments. Geochronometria 25 (5), 77–94. https://doi.org/10.1016/j.geobios.2004.10.004.
Slatt, R.M., O'Brien, N.R., 2011. Pore types in the Barnett and Woodford gas shales: contribution to understanding gas storage and migration pathways in fine-grained rocks. Am. Assoc. Petrol. Geol. Bull. 95 (12), 2017–2030. https://doi.org/10.1306/03301110145.
Sone, H., Zoback, M.D., 2013. Mechanical properties of shale-gas reservoir rocks — Part 1: static and dynamic elastic properties and anisotropy. Geophysics 78 (5), 381–392. https://doi.org/10.1190/geo2013-0050.1.
Su, W.B., Li, Z.M., Ettensohn, F.R., Johnson, M.E., Huff, W.D., Wang, W., Ma, C., Li, L., Zhang, L., Zhao, H.J., 2007. Distribution of black shale in the Wufeng-Longmaxi Formations (Ordovician-Si-lurian), South China: major controlling factors and implications. Earth Sci. J. China Univ. Geosci. 32 (6), 819–827. https://doi.org/10.3321/j.issn:1000-2383.2007.06.013 (in Chinese with English abstract).
Tian, H., Pan, L., Xiao, X.M., Wilkins, R.W.T., Meng, Z.P., Huang, B.J., 2013. A preliminary study on the pore characterization of Lower Silurian black shales in the Chuandong thrust fold belt, southwestern China using low pressure Na adsorption and FE-SEM Methods. Mar. Petrol. Geol. 48, 8–19. https://doi.org/10.1016/j.marpetgeo.2013.07.008.
Tribovillard, N., Petit, A., Quijada, M., Riboulleau, A., Averbuch, O., 2018. A genetic link between synsedimentary tectonics-expelled fluids, microbial sulfate reduction and cone-in-cone structures. Mar. Petrol. Geol. 93, 437–450. https://doi.org/10.1016/j.marpetgeo.2018.03.024.
Tucker, M.E., 1982. Precambrian dolomites: petrographic and isotopic evidence that they differ from Phanerozoic dolomites. Geology 10 (1), 7–12. https://doi.org/10.1130/0091-7613(1982)10<7:PDPAIE>2.0.CO;2.
Wang, M., Chen, Y., Song, G.Q., Steele-MacInnis, M., Liu, Q., Wang, X.J., Zhang, X.J., Zhao, Z.Y., Liu, W.Y., Zhang, H.J., Zhou, Z.Z., 2018. Formation of bedding-parallel, fibrous calcite veins in laminated source rocks of the Eocene Dongying Depression: a growth model based on petrographic observations. Int. J. Coal Geol. 200, 18–35. https://doi.org/10.1016/j.coal.2018.10.004.
Wang, S.F., Zou, C.N., Dong, D.Z., Wang, Y.M., Huang, J.L., Guo, S.J., 2014a. Biogenic silica of organic-rich shale in Sichuan Basin and its significance for shale gas. Acta Sci. Nauralium Univ. Pekin. 50 (3), 476–486. https://doi.org/10.13209/j.0479-8023.2014.079 (in Chinese with English abstract).
Wang, S., Javadpour, F., Feng, Q.H., 2016. Confinement correction to mercury intrusion capillary pressure of shale nanopores. Sci. Rep. 6 (1), 1–12. https://doi.org/10.1038/srep20160.
Wang, X., Gao, J., He, S., He, Z.L., Zhou, Y., Tao, Z., Zhang, J.K., Wang, Y., 2017. Fluid inclusion and geochemistry studies of calcite veins in Shizhu synclinorium, central China: record of origin of fluids and diagenetic conditions. J. Earth Sci. 28 (2), 315–332. https://doi.org/10.1007/s12583-016-0921-7.
Wang, Y.M., Dong, D.Z., Yang, H., He, L., Wang, S., Huang, J., Pu, P., Wang, S., 2014b. Quantitative characterization of reservoir space in the lower Silurian Longmaxi Shale , southem Sichuan, China. Sci. China Earth Sci. 57 (2), 1348–1356. https://doi.org/10.1007/s11430-013-4645-y (in Chinese with English abstract).

Washburn, E.W., 1921. Note on a method of determining the distribution of pore sizes in porous materials. Proc. Natl. Acad. Sci. USA 7 (4), 115–116. https://doi.org/10.1073/PNAS.7.4.115.

Wright, D.T., Wacey, D., 2005. Precipitation of dolomite using sulphate-reducing bacteria from the Coorong Region, South Australia: significance and implications. Sediment 52 (5), 987–1008. https://doi.org/10.1111/j.1365-3091.2005.00732.x.

Yang, R., He, S., Yi, J.Z., Hu, Q.H., 2016. Nano-scale pore structure and fractal dimension of organic-rich Wufeng-Longmaxi shale from Jiaoshiba area, Sichuan basin: investigations using FE-SEM, gas adsorption and helium pycnometry. Mar. Petrol. Geol. 70, 27–45. https://doi.org/10.1016/j.marpetgeo.2015.11.019.

Yang, T., Cao, Y.C., Friis, H., Liu, K.Y., Wang, Y.Z., Zhou, L., Zhang, S., Zhang, H., 2018. Genesis and distribution pattern of carbonate cements in lacustrine deep-water gravity-flow sandstone reservoirs in the third member of the Shahejie Formation in the Dongying Sag, Jiyang Depression, Eastern China. Mar. Petrol. Geol. 92, 547–564. https://doi.org/10.1016/j.marpetgeo.2017.11.020.

Yuan, Y.J., Rezaee, R., Yu, H.Y., Zou, J., Liu, K.Q., Zhang, Y.H., 2021. Compositional controls on nanopore structure in different shale lithofacies: a comparison with pure clays and isolated kerogens. Fuel 303, 121079. https://doi.org/10.1016/j.fuel.2021.121079.

Yuan, Y.J., Rezaee, R., Gu, J.W., Wu, S.T., Al-Khdheeawi, E.A., Wang, J., Pan, B., 2023. High-resolution coupling of stratigraphic sweet spot lithofacies and petrophysical properties: a multiscale study of Ordovician Goldwyer Formation, Western Australia. Petrol. Sci. 20 (3), 1312–1326. https://doi.org/10.1016/j.petsci.2022.11.001.

Zan, B., Mou, C.L., Lash, G.G., Yan, J.X., Hou, Q., 2022. Diagenetic barite-calcite-pyrite nodules in the Silurian Longmaxi Formation of the Yangtze Block, South China: a plausible record of sulfate-methane transition zone movements in ancient marine sediments. Chem. Geol. 595, 120789. https://doi.org/10.1016/j.chemgeo.2022.120789.

Zou, C.N., Dong, D.Z., Wang, S.J., Li, J.Z., Wang, Y.M., Li, D.H., Cheng, K.M., 2010. Geological characteristics, formation mechanism and resource potential of shale gas in China. Petrol. Explor. Dev. 37 (6), 641–653. https://doi.org/10.1016/S1876-3804(11)60001-3 (in Chinese with English abstract).

Zou, C.N., Dong, D.Z., Wang, Y.M., Li, X.J., Huang, J.L., Wang, S.F., Guan, Q.Z., Zhang, C.C., Wang, H.Y., Liu, H.L., Bai, W.H., Liang, F., Lin, W., Zhao, Q., Liu, D.X., Yang, Z., Liang, P.P., Sun, S.S., Qiu, Z., 2015. Shale gas in China: characteristics, challenges and prospects (I). Petrol. Explor. Dev. 42 (2), 689–701. https://doi.org/10.1016/S1876-3804(16)30022-2 (in Chinese with English abstract).

Zhang, J.G., Jiang, Z.X., Jiang, X.L., Wang, S.Q., Liang, C., Wu, M.H., 2016. Oil generation induces sparry calcite formation in lacustrine mudrock, Eocene of East China. Mar. Petrol. Geol. 71, 344–359. https://doi.org/10.1016/j.marpetgeo.2016.01.007.

Zhao, J.H., Jin, Z.J., Jin, Z.K., Wen, X., Geng, Y.K., Yan, C.N., Nie, H.K., 2016a. Lithofacies types and sedimentary environment of shale in Wufeng-Longmaxi formation, Sichuan Basin. Aeta Pet. Sin. 37 (5), 572–586. https://doi.org/10.7623/syxb201605002 (in Chinese with English abstract).

Zhao, J.H., Jin, Z.J., Jin, Z.K., Geng, Y.K., Wen, X., Yan, C.N., 2016b. Applying sedimentary geochemical proxies for paleoenvironment interpretation of organic-rich shale deposition in the Sichuan Basin, China. Int. J. Coal Geol. 163, 52–71. https://doi.org/10.1016/j.coal.2016.06.015.

Zhao, J.H., Jin, Z.J., 2021. Mudstone diagenesis: research advances and prospects. Acta Sedimentol. Sin. 39 (1), 58–72. https://doi.org/10.14027/J.ISSN.1000-0550.2020.133 (in Chinese with English abstract).

Zheng, Y.J., Liao, Y.H., Wang, Y.P., 2022. The main geological factors controlling the Wufeng-Longmaxi shale gas content. Am. Assoc. Petrol. Geol. Bull. 106 (10), 2073–2102. https://doi.org/10.1306/07132218243.

Zhou, X.F., Li, X.Z., Guo, W., Zhang, X.W., Liang, P.P., Yu, J.M., 2022. Characteristics, formation mechanism and influence on physical properties of carbonate minerals in shale reservoir of Wufeng-Longmaxi Formations, Sichuan Basin. Nat. Gas Geosci. 7 (3), 133–146. https://doi.org/10.1016/j.jnggs.2022.07.001 (in Chinese with English abstract).